Quantum coherent spin-electric control in a molecular nanomagnet at clock transitions

Junjie Liu,[1,*] Jakub Mrozek,[1] Aman Ullah,[2] Yan Duan,[2] José J. Baldoví,[2] Eugenio Coronado,[2] Alejandro Gaita-Ariño,[2,†] and Arzhang Ardavan[1,‡]

[1] *CAESR, Department of Physics, University of Oxford, The Clarendon Laboratory, Parks Road, Oxford OX1 3PU, UK*

[2] *Instituto de Ciencia Molecular (ICMol), Universitat de València, Paterna, Spain*

Abstract

Electrical control of spins at the nanoscale offers significant architectural advantages in spintronics, because electric fields can be confined over shorter length scales than magnetic fields [1–5]. Thus, recent demonstrations of electric-field (E-field) sensitivities in molecular spin materials [6–8] are tantalising, raising the viability of the quantum analogues of macroscopic magneto-electric devices [9–15]. However, the E-field sensitivities reported so far are rather weak, prompting the question of how to design molecules with stronger spin-electric couplings. Here we show that one path is to identify an energy scale in the spin spectrum that is associated with a structural degree of freedom with a significant electrical polarisability. We study an example of a molecular nanomagnet in which a small structural distortion establishes clock transitions (i.e. transitions whose energy is to first order independent of magnetic field) in the spin spectrum; the fact that this distortion is associated with an electric dipole allows us to control the clock transition energy to an unprecedented degree. We demonstrate coherent electrical control of the quantum spin state and exploit it to manipulate independently the two magnetically-identical but inversion-related molecules in the unit cell of the crystal. Our findings pave the way for the use of molecular spins in quantum technologies and spintronics.

* junjie.liu@physics.ox.ac.uk

† Alejandro.Gaita@uv.es

‡ arzhang.ardavan@physics.ox.ac.uk

The polyoxometalate molecular anion $[Ho(W_5O_{18})_2]^{9-}$ (abbreviated to HoW_{10}), within the crystal structure $Na_9[Y_{1-x}Ho_x(W_5O_{18})_2)]\cdot 35H_2O$ ($x = 0.1\%$), provides an example of clock transition (CT) molecular spin qubit [16, 17]. In the solid state, the sodium salt of this anion crystallizes in a primitive space group of $P\bar{1}$, where each unit cell contains two HoW_{10} anions that are inversion-symmetry related. Each HoW_{10} possesses an approximate D_{4d} symmetry. The magnetic properties of the HoW_{10}, which are characterised by a total electronic angular momentum of $J = 8$ and a nuclear spin of $I = 7/2$, can be described by the Hamiltonian [18]

$$\begin{aligned}\hat{H} = &\sum_{k=2,4,6}\sum_{q=-k}^{k} B_k^q \hat{O}_k^q + \hat{J}\cdot A\cdot \hat{I} \\ &+\mu_B g_e \boldsymbol{B}_0\cdot\hat{J} - \mu_N g_N \boldsymbol{B}_0\cdot\hat{I}\end{aligned} \tag{1}$$

where A is the magnitude of the (approximately) isotropic hyperfine interaction, g_e and g_N are the electronic and nuclear gyromagnetic ratios respectively, the anisotropy is parameterised by the amplitudes B_k^q of the extended Stevens operators $\hat{O}_k^q$, and $\boldsymbol{B}_0$ is the applied magnetic field.

The crystal field terms $\sum_k B_k^0 \hat{O}_k^0$ lead to a ground state of $m_J = \pm 4$, where m_J is the projection of the electronic angular momentum. Crucially, owing to interactions of HoW_{10} with counterions and crystallisation water, there is a minor deviation from ideal D_{4d} symmetry, with a continuous-shape measurement $S < 0.1$ around the Ho^{3+} ion as defined by SHAPE [19, 20]. Specifically, the chemical structure shows that the skew angle, θ, deviates from the ideal value of 45°, and that the Ho^{3+} centre deviates from the centre position by a distance of $d = (h - h')/2$. The latter indicates that the Ho^{3+} is closer to one of the two $[W_5O_{18}]^{6-}$ moieties. The crystal structures measured at three different temperatures (100K, 150K, and 200K) are provided in Ref [19] (see Section II). At these three temperatures, the deviations of the skew angles are 2.21°, 2.34° and 2.27°, whereas the off-centre distances are 0.021 Å, 0.025 Å and 0.024 Å, respectively.

This gives rise to an electric dipole moment and a tetragonal spin anisotropy (parameterised by terms B_k^4) which mixes the $m_J = \pm 4$ ground states and generates a series of anti-crossings in the ground spin spectrum, leading to four electron spin resonance (ESR) CTs, whose resonance frequencies are determined by the amplitude of the tetragonal anisotropy. The four CTs correspond to resonances with different electron–nuclear spin states $|m_J, m_I\rangle$ with $m_J = \pm 4$ and of m_I = -1/2, -3/2, -5/2 or -7/2 (from low to high fields). Previ-

FIG. 1. (a) HoW_{10} (left) and the coordination environment for the Ho^{3+} (right). A small rotation of the two Ho-coordinated $[W_5O_{18}]^{6-}$ ligands (θ) and displacement of Ho ($h \neq h'$) give rise to a tetragonal anisotropy. (b) Schematic plot showing the experiment configuration. The electric field was generated by applying voltage pulses to two parallel conducting plates. The magnetic field was applied parallel to the z-axis (in the $x-y-z$ laboratory frame). The sample was oriented to minimize the angle between the molecular easy axis (the red arrow in the $x-z$ plane) and $\boldsymbol{B}_0$ (estimated misalignment $\beta \sim 38°$). The E-field orientation φ was rotated within the $y-z$ plane. (c) E-field effect on the spin echo of HoW_{10} measured at $B_0 = 0.0304$ T. The in-phase part of the integrated echo intensity oscillates strongly as a function of the duration (t_E) of the E-field pulse generated by applying a voltage of 300 V. By comparison, the quadrature component (red line) remains flat at zero throughout the experiment. The durations of the $\pi/2$ and π microwave pulses were 32 and 64 ns respectively, and the separation between them was fixed at 6 μs. All the SEC measurements presented in this work (except the selective spin excitation data shown in Fig. 3) were conducted using the same protocol and the shift in the ESR frequency, δf, is obtained by Fourier transforming the oscillating in-phase component of the spin echo.

ous ESR and magnetization studies [17, 18] are satisfactorily simulated by the parameters $B_2^0/h = 18.0 \times 10^3$ MHz, $B_4^0/h = 209$ MHz, $B_6^0/h = 1.53$ MHz, $B_4^4/h = 94.2$ MHz, $A/h = 830$ MHz and $g_e = 1.25$.

Thus the broken inversion symmetry causes the spin-electric coupled phenomena of an electric dipole and a clock transition. This, in turn, allows us to manipulate the CT frequency linearly by applying an external electric field (E-field).

We investigated the spin-electric coupling (SEC) in HoW_{10} by embedding E-field pulses in an ESR Hahn-echo sequence, as described in Refs [6, 19] and Methods. Fig. 1c shows typical data recorded with the E-field applied parallel to $\boldsymbol{B}_0$, $\varphi = 0$. The in-phase part of spin echo shows a pronounced oscillation upon varying the length of the E-field pulse. The oscillation arises because the molecular spin Hamiltonian is modulated by the E-field via the SEC, leading to a shift δf of the ESR frequency while the E-field is applied. This shift in the ESR frequency manifests as an additional phase of $\delta f \cdot t_E$ in the spin echo signal, causing the oscillation of period 1 μs in the echo amplitude (see Supplementary Figure S1). The decay in the echo amplitude over $0 < t_E \leq 6$ μs is due to a small inhomogeneity in the

FIG. 2. (a) Orientation dependence of the E-field induced frequency shift. The measurements were performed with $f = 9.15$ GHz , $V = 300$ V and $B_0 = 0.0304$ T. The E-field was rotated between parallel to $\boldsymbol{B}_0$ (i.e. 38° away the molecular easy-axis) at $\varphi = 0$ (180°) and perpendicular to $\boldsymbol{B}_0$ (i.e. in the molecular hard plane), $\varphi = 90°$. (b) The measured frequency shift (□) versus the applied voltage, V, showing a linear E-field coupling in HoW_{10}. The data were recorded at the orientation with the strongest SEC ($\varphi = 145°$). The red line is a linear fit to the data. Blue lines represent the *ab initio* prediction based on molecular geometry extracted from (solid) single-crystal X-ray crystallography or (dashed) structure fully optimsed at DFT level (see details in Ref [19]). Inset: the local environment of the Ho showing the electric dipole direction (magenta arrow) and the E-field-induced atomic displacement directions (orange arrows). (c) ESR spectra recorded at various frequencies close to the CT frequency. (d) The E-field effect measured on the corresponding ESR transitions. The dashed lines illustrate the E-field-induced frequency shift δf expected if only B_4^4 were modified by the E-field; the scatter in δf at frequencies away from the clock transition indicates that the E-field-sensitivity of other Hamiltonian terms becomes important. The error bars for δf in (a) and (b) are approximately equal to the size of the symbols (not shown).

E-field across the crystal; during the second period of free evolution 6 μs $< t_{\mathrm{E}} \leq 12$ μs, the inhomogeneity is refocused and the echo amplitude recovers [6].

The lack of a dependence of the quadrature channel of the echo on t_{E} is evidence of a linear, as opposed to quadratic, SEC in HoW_{10}. The crystal unit cell contains two HoW_{10} units related by inversion symmetry; a linear SEC shifts the ESR frequency of each by the same amount but in opposite directions. Hence the phase shifts for the spin echoes of the two inequivalent spins are $+\delta f \cdot t_{\mathrm{E}}$ and $-\delta f \cdot t_{\mathrm{E}}$ respectively, and the quadrature part of the combined echo signal remains zero, independent of t_{E}. For a second order SEC $\delta f \propto E^2$, both spins in the unit cell acquire the same phase, because the shift is insensitive to the polarity of the E-field. Thus an oscillation in the quadrature component, $\pi/2$ out of phase with the in-phase component, is a signature of a second-order SEC [21].

The orientation dependence of the SEC is shown in Figure 2a. The shift in the ESR frequency δf is calculated by taking the fast Fourier transform of the oscillation in the in-phase echo intensity. It depends on orientation as $|\delta f| \propto |\cos\varphi - \varphi_0|$ (the presence of both inversion-related populations means that we cannot distinguish the sign of δf from

this measurement). This yields a lower bound on the scale of the SEC; a full mapping of the SEC orientation dependence would be required to establish the orientation with maximum E-field sensitivity. This would depend on two-axis rotation of the electric field, which is beyond the scope of this study.

The linearity of the SEC is further confirmed by varying the amplitude of the E-field pulse of fixed duration. Figure 2b demonstrates that the frequency shift is proportional to the voltage (and hence, since the electrode geometry is fixed, the amplitude of the E-field). The data were recorded at the orientation φ that shows the strongest SEC. The linear fit to the data yields a spin-electric coupling constant of 11.4 ± 0.3 Hz/Vm^{-1}.

The relative strength of the SEC in HoW_{10} showcases the potential for chemical design in enhancing desired molecular properties via prudent choice of the coordination environment of the metal ion. Such engineering is not possible in, for example, atomic defects in solid state materials, in which structures and therefore properties are much less tunable. Furthermore, the possibility of tuning the ESR transition at the CT fields allows the exploitation of the strong spin orbit coupling characteristic of $4f$ electrons to enhance the electrical control of molecular qubits, while retaining substantial coherence times. Such tuning of the HoW_{10} CT can only be achieved efficiently by directly adjusting the tetragonal anisotropy interaction since, at the CT fields, the ESR transitions are insensitive to g_e or A to first order [19].

The ESR frequency at the CT fields is determined by the tetragonal anisotropy. Therefore, all ESR transitions at 9.15 GHz exhibit the same response to the applied electric fields (filled squares in Fig. 2d) and can be fitted with a $\delta B_4^4/h = 8.8 \pm 0.2 \times 10^{-3}$ MHz (5.9×10^{-2} Hz/Vm^{-1}). However, other spin Hamiltonian terms, such as Zeeman and hyperfine interactions, may potentially also exhibit E-field sensitivities. These interactions modify the ESR transition frequencies away from the CT fields; we can probe their sensitivities by studying the E-field effect on ESR transitions away from the CT fields, as shown in Fig. 2c and d.

The E-field-induced ESR frequency shift decreases as the ESR frequency increases, which is expected as the "anticrossing" effect of B_4^4 reduces when moving away from the CTs. On the other hand, the SEC effects also fluctuate considerably from peak to peak at 9.45 and 9.88 GHz. Such fluctuation is likely due to the E-field modulation of Hamiltonian parameters other than B_4^4: the appreciable dependence of δf on magnetic field and nuclear spin projection away from the CT fields (i.e. between states with varying contributions from

different nuclear spin projections m_I and electron spin projections m_J) suggest that Zeeman and hyperfine interactions may also be sensitive to the E-field, though less so than B_4^4 [19].

We seek insight into the relationship between the E-field-induced distortion and the CT frequency by noting that any molecular distortion may be decomposed into displacements of the normal modes of the HoW_{10}, which we obtain using density functional theory (DFT, implemented by Gaussian [22]). Each normal mode is associated with a force constant κ_i and a reduced mass μ_i (yielding an eigenfrequency $\omega_i = \sqrt{\kappa_i/\mu_i}$). The electric dipole $\boldsymbol{p}$ depends on the displacement of the mode x_i, and this determines the coupling of the mode to an applied E-field or to incident light, i.e. its infrared (IR) intensity.

When an external electric field $\boldsymbol{E}$ is incremented by $\mathrm{d}\boldsymbol{E}$, it elastically distorts the molecule by $\mathrm{d}x_i$ and modifies the molecular electric dipole by $\mathrm{d}\boldsymbol{p}_i$ for mode i. In this process, it does work $\boldsymbol{E} \cdot \sum_i \mathrm{d}\boldsymbol{p}_i = \sum_i \kappa_i \, \mathrm{d}x_i$. Thus by calculating the electric dipole moment as a function of the mode displacements, we can extract quantitatively the displacements as a function of applied E-field, and hence the electric-field-induced evolution of the molecular electronic structure (see Methods).

This reasoning yields criteria by which we may determine whether a particular molecular mode leads to a strong contribution to the SEC at the CT frequency: it should be relatively soft (i.e. exhibit small κ_i), allowing a significant molecular displacement without excessive elastic energy cost; it should couple strongly to the molecular electric dipole (i.e. $\mathrm{d}\boldsymbol{p}_i/\mathrm{d}x_i$, and therefore its IR intensity, should be large); and it should modify the Ho environment such that the energy of the anticrossing levels is modulated. Our analysis of the basis of the HoW_{10} vibrational modes of the crystallographic structure reveals that the molecular displacement responsible for the SEC can be approximated by the distortion displacing the Ho and coordinating oxygen atoms as shown in the inset to Fig. 2(b). The analysis based on the relaxed structure yields a very similar result. Animations showing each of these collective distortions are available as SI files. The difference between the SECs predicted using the optimised and the crystal structures (blue dashed/solid lines in Fig. 2b) can be understood by considering how the structure deviates from the ideal D_{4d} symmetry. A departure from the D_{4d} structure, which is inversion symmetric, is necessary to afford a linear SEC in HoW_{10}. Compared to the optimised molecular geometry, the actual crystal structure shows a larger distortion due to the presence of the Na^+ counterions and crystallisation H_2O molecules. Therefore, it is conceivable that the optimised structure leads to an underestimation of the

FIG. 3. (a) The modified Hahn-echo pulse sequence used for selective spin excitation. A $\pi/2$ pulse is applied at the CT frequency f_0, while the frequency of the refocusing π pulse, $f_{\rm r}$, is swept. An E-field square pulse is applied simultaneously with the refocussing pulse to modulate the excitation frequencies of molecular spins. When $f_{\rm r} = f_0 \pm \delta f$, the refocusing pulse selectively inverts one or other of the inversion-symmetry-related molecular spins in the unit cell. (b) The intensity of the spin echo as a function of the applied voltage, V, and the frequency offset of the refocusing pulse, $\delta f = f_0 - f_r$.

SEC. Nevertheless, the theoretical results are in reasonable agreement with the experimental data.

We note in passing that, from a practical perspective, any external electric field that can be applied experimentally is very small compared to the intra-molecular fields associated with chemical bonds, justifying our perturbative approach. Others have investigated the effects of electric fields on the $\sim 10\,\mathrm{V/nm}$ scale on lanthanide single-ion molecular magnets, a regime that can be explored directly in DFT [25].

Finally, we demonstrate a protocol to selectively manipulate the spins of inversion-related HoW_{10} anions assisted by an E-field [1, 3]. Since the two spins within the unit cell are related by inversion symmetry, they are magnetically identical and cannot be distinguished in conventional ESR or magnetometry experiments. However, they exhibit opposite frequency shifts in the presence of an E-field, which can be exploited, using a modified Hahn-echo sequence as shown in Figure 3a, to excite them selectively. The first pulse, a $\pi/2$ pulse at the CT frequency of $f_0 = 9.15$ GHz, places all molecular spins in a superposition state. An E-field is applied simultaneously with the refocusing π pulse, lifting the degeneracy of the ESR transitions in the two inversion-related populations. Thus it is possible to refocus only one subpopulation, as long as (i) the π pulse is resonant with the shifted ESR frequency of that subpopulation, and (ii) the shift is larger than the natural line width of the excited spin population. The echo that forms following the second period of free evolution is detected at the frequency f_0, but is comprised only of the spins from the refocused subpopulation.

We set the durations of the $\pi/2$ and π microwave pulses to be 400 ns and 800 ns respectively, to selectively excite a narrow frequency population of spins. (Note that these pulses are more than ten times longer than those used in the preceding experiments, and

therefore drive a correspondingly narrower range of ESR transition frequencies.) Figure 3b shows a density plot of the echo amplitude as a function of the applied voltage V and the frequency offset of the refocusing pulse $\delta f = f_0 - f_r$ (see section VI in Ref [19] for more data). In the absence of an E-field pulse ($V = 0$), the maximum echo signal is observed when the frequencies of the $\pi/2$ and π pulses are identical, i.e. $\delta f = 0$. Upon increasing the amplitude of the E-field, subpopulations are refocused for two different values of δf, and these subpopulations are spectrally well-resolved for $V > 150$ V.

The offset is in excellent agreement with the expected SEC for HoW_{10} and the echo signal peaks at the symmetric positions $\pm\delta f$ around $\delta f = 0$, corresponding to the selective refocusing of the inversion-related subpopulations. Furthermore, the echo intensities at $\pm\delta f$ are identical and approximately half of the intensity in the absence of an electric field, indicating that only half of the population is refocused, and that the refocusing is equally effective for both subpopulations. This demonstrates that, with the assistance of an electric field, we can distinguish orientations of otherwise magnetically identical HoW_{10} units.

As is generally the case in quantum information experiments, strong coupling to a control field means strong coupling to a source of noise that shares the same physics as the control. In the case described here, we reduce sensitivity to magnetic fields by working at a CT, but this in turn increases sensitivity to molecular distortions and E-field fluctuations. We note, however, that reducing temperature (which will in any case be required for initialisation) suppresses environmental phonons (the principal source of molecular distortions), but cannot remove all magnetic field fluctuations, which may have their origin in, for example, environmental spin flip-flop processes [26].

Our results guide us to distill the general recipe for a high-SEC-molecule: a soft and electrically polarisable environment for the spin carriers, and a spin spectrum that is highly sensitive to distortions. These principles are satisfied in HoW_{10}, where a clock transition frequency is modulated by soft modes that shift the molecular charge distribution. The SEC is about an order of magnitude larger than the values the previously reported for transition-metal-based molecular nanomagnets [6, 7, 27] ($\delta f/E < 1$ Hz/Vm^{-1}) and it also surpasses the SEC measured for rare earth atoms doped in YAG [28] ($\delta f/E \approx 1$ Hz/Vm^{-1}). It is similar to the SEC for Mn^{2+} in ZnO [29] ($\delta f/E = 12.7$ and 6.4 Hz/Vm^{-1} for $m_s : \pm 5/2 \leftrightarrow \pm 3/2$ and $\pm 3/2 \leftrightarrow \pm 1/2$ transitions, respectively), in which the SEC is associated with the piezoelectric nature of the host lattice. The HoW_{10} coupling is sufficiently strong that a

modest E-field of $\sim 10^5$ V/m or 100 μV/nm is adequate to tune the spin at a practically useful level, i.e. to shift the frequency by much more than the natural line width; this demonstrates the principle that local E-field tuning allows for selective addressing of spins in otherwise identical molecules. The strong SEC in HoW_{10} raises the tantalizing possibility of engineering a coherent spin-photon interface in molecular spintronic devices [30], allowing coherent spin control by an oscillating electric field [5]. These results pave the way for the use of molecular components in quantum or classical spintronic technologies in which local electrical control can surpass the performance of conventional magnetic spin control.

Methods

ESR apparatus and sample configuration The HoW_{10} crystal was mounted in a 1.6 mm outer diameter ESR quartz tube and inserted between parallel metallized plates separated by 2 mm, which were used to apply E-field pulses. Both the conductive plates and the sample were mounted in a standard Bruker MD5 resonator and could be rotated independently around the x-axis as shown in Fig. 1b. By first studying the clock transition fields as a function of the sample rotation, we were able to determine the angle between the magnetic easy axis and the experimental rotation axis. In all experiments presented in this study, the magnetic easy axis was aligned as close as possible to $\boldsymbol{B}_0$. We applied the E-field at a variable orientation φ with respect to $\boldsymbol{B}_0$ (Fig. 1b).

Note that the magnetic easy axis is not coincident with any of the crystal facets or edges [17, 18], nor is it collinear with the pseudo-four-fold molecular symmetry axis, so it is not possible to guarantee the alignment by inspecting the crystal morphology. Thus repeating the experiment on a different crystal gives a similar orientation dependence for the SEC, albeit the extrema of the SEC appear at different laboratory directions (see Ref [19], Section IV). This cosine-shaped orientation dependence of the SEC is indicative of the existence of an axial-type SEC in HoW_{10}. The differences in behaviour between the two crystals arise from the variation in orientation of the crystals in the apparatus, and therefore the plane through which they are rotated in the laboratory frame (see Ref [19] Section V for more details).

Microwave pulse sequences A standard two-pulse Hahn-echo sequence ($\pi/2 - \tau - \pi - \tau$ – echo) was employed to measure an electron spin echo on the HoW_{10} crystals. Short broadband pulses, 32 ns for $\pi/2$-pulses and 64 ns for π-pulses, were used for measuring the SEC parameters (data shown in Figs. 1 and 2). These pulse parameters were adjusted in order to optimise the echo intensity. By contrast, long selective pulses, 400 ns for $\pi/2$-pulses and 800 ns for π-pulses, were applied in the selective spin manipulation experiments (Fig. 3). These pulse lengths were chosen to excite a narrow frequency population of spins, which can be selectively manipulated using the E-field-induced frequency shift, while still giving a reasonable signal-to-noise ratio in spin echo measurements.

Calculation of SEC The E-field-induced change in the clock transition frequency is evaluated by computing the evolution of the molecular electronic structure using the multireference Complete Active Self-Consistent Field Spin-Orbit (CASSCF-SO) method (implemented by OpenMOLCAS [23]) with the combined effect of the crystal field and the spin-orbit coupling calculated using SINGLE-ANISO module [24]. The effect of the E-field on the easy axis orientation was also estimated (for details, see Ref [19] Section VIII). The theory study was performed using both the crystal structure obtained and the relaxed structure optimised at the DFT level.

Data Availability Statement Experimental data supporting the conclusions are available at `https://doi.org/10.5281/zenodo.5167019`.

Acknowledgements

This work is supported by: the EU (ERC-2014-CoG-647301 DECRESIM, ERC-2018-AdG-788222 MOL-2D, COST Action CA15128 MOLSPIN, the QuantERA project SUMO, and the H2020 research and innovation programme projects SPRING (No 863098) and FATMOLS (No 862893)); the Spanish MINECO (grant CTQ2017-89993 co-financed by FEDER, grant MAT2017-89528; the Unit of excellence "María de Maeztu" CEX2019-000919-M); the Generalitat Valenciana (Prometeo Program of Excellence); and the UK EPSRC (EP/P000479/1). J.J.B. acknowledges support by the Generalitat Valenciana (CDEIGENT/2019/022). J.M. is supported by Magdalen College, Oxford. J.L. is supported by the Royal Society through a University Research Fellowship.

Author Contributions

J.L., E.C., A.G.-A. and A.A. conceived the study. Materials were synthesised by Y.D. under the supervision of E.C. ESR experiments were conducted by J.L. and J.M. Data analysis was

performed by J.L. with input from A.A. Theoretical modelling was done by A.U., assisted by J.J.B, guided by A.G.-A., and in discussion with J.L., E.C. and A.A. All authors contributed to the manuscript.

Competing Interests

The authors declare no competing interests.

Additional Information

Supplementary Information is available for this paper.

---

[1] Kane, B. E. A silicon-based nuclear spin quantum computer. *Nature* **393**, 133–137 (1998). URL http://www.nature.com/doifinder/10.1038/30156.

[2] Trif, M., Troiani, F., Stepanenko, D. & Loss, D. Spin-Electric Coupling in Molecular Magnets. *Physical Review Letters* **101**, 217201 (2008). URL https://link.aps.org/doi/10.1103/PhysRevLett.101.217201.

[3] Laucht, A. *et al.* Electrically controlling single-spin qubits in a continuous microwave field. *Science Advances* **1**, e1500022–e1500022 (2015). URL http://advances.sciencemag.org/cgi/doi/10.1126/sciadv.1500022.

[4] Tosi, G. *et al.* Silicon quantum processor with robust long-distance qubit couplings. *Nature Communications* **8**, 450 (2017). URL http://www.nature.com/articles/s41467-017-00378-x.

[5] Asaad, S. *et al.* Coherent electrical control of a single high-spin nucleus in silicon. *Nature* **579**, 205–209 (2020). URL http://www.nature.com/articles/s41586-020-2057-7.

[6] Liu, J. *et al.* Electric Field Control of Spins in Molecular Magnets. *Physical Review Letters* **122**, 037202 (2019). URL https://link.aps.org/doi/10.1103/PhysRevLett.122.037202.

[7] Fittipaldi, M. *et al.* Electric field modulation of magnetic exchange in molecular helices. *Nature Materials* **18**, 329–334 (2019). URL http://www.nature.com/articles/s41563-019-0288-5.

[8] Robert, J., Parizel, N., Turek, P. & Boudalis, A. K. Polyanisotropic Magnetoelectric Coupling in an Electrically Controlled Molecular Spin Qubit. *Journal of the American Chemical Society* **141**, 19765–19775 (2019). URL https://pubs.acs.org/doi/10.1021/jacs.9b09101.

[9] Palii, A., Clemente-Juan, J. M., Tsukerblat, B. & Coronado, E. Electric field control of

the optical properties in magnetic mixed-valence molecules. *Chemical Science* **5**, 3598–3602 (2014). URL http://xlink.rsc.org/?DOI=C4SC01056F.

[10] Cardona-Serra, S. *et al.* Electrically Switchable Magnetic Molecules: Inducing a Magnetic Coupling by Means of an External Electric Field in a Mixed-Valence Polyoxovanadate Cluster. *Chemistry - A European Journal* **21**, 763–769 (2015). URL http://doi.wiley.com/10.1002/chem.201404055.

[11] Gaita-Ariño, A., Luis, F., Hill, S. & Coronado, E. Molecular spins for quantum computation. *Nature Chemistry* **11**, 301–309 (2019). URL http://www.nature.com/articles/s41557-019-0232-y.

[12] Atzori, M. & Sessoli, R. The Second Quantum Revolution: Role and Challenges of Molecular Chemistry. *Journal of the American Chemical Society* **141**, 11339–11352 (2019). URL https://pubs.acs.org/doi/10.1021/jacs.9b00984.

[13] Godfrin, C. *et al.* Operating Quantum States in Single Magnetic Molecules: Implementation of Grover's Quantum Algorithm. *Physical Review Letters* **119**, 187702 (2017). URL https://link.aps.org/doi/10.1103/PhysRevLett.119.187702.

[14] Eerenstein, W., Mathur, N. D. & Scott, J. F. Multiferroic and magnetoelectric materials. *Nature* **442**, 759–765 (2006). URL http://www.nature.com/articles/nature05023.

[15] Matsukura, F., Tokura, Y. & Ohno, H. Control of magnetism by electric fields. *Nature Nanotechnology* **10**, 209–220 (2015). URL http://www.nature.com/articles/nnano.2015.22.

[16] AlDamen, M. A. *et al.* Mononuclear Lanthanide Single Molecule Magnets Based on the Polyoxometalates $[Ln(W_5O_{18})_2]^{9-}$ and $[Ln(\beta_2\text{-}SiW_{11}O_{39})_2]^{13-}$ (Ln^{III} = Tb, Dy, Ho, Er, Tm, and Yb). *Inorganic Chemistry* **48**, 3467–3479 (2009). URL https://pubs.acs.org/doi/10.1021/ic801630z.

[17] Shiddiq, M. *et al.* Enhancing coherence in molecular spin qubits via atomic clock transitions. *Nature* **531**, 348–351 (2016). URL http://www.nature.com/doifinder/10.1038/nature16984.

[18] Ghosh, S. *et al.* Multi-frequency EPR studies of a mononuclear holmium single-molecule magnet based on the polyoxometalate $[Ho]^{III}(W_5O_{18})_2]^{9-}$. *Dalton Transactions* **41**, 13697 (2012). URL http://xlink.rsc.org/?DOI=c2dt31674a.

[19] See Supplemental Material for detailed information on methods, calculations and ancillary

experiments.

[20] Alvarez, S., Alemany, P., Casanova, D., Cirera, J. & Llunell, M. Shape maps and polyhedral interconversion paths in transition metal chemistry. *Coordination Chemistry Reviews* **249**, 1693–1708 (2005).

[21] An oscillation in the quadrature component can also arise if the E-field pulse is accompanied by a parasitic magnetic field pulse that distorts $\boldsymbol{B}_0$; it contributes a trivial phase to the echo via the Zeeman interaction.

[22] Frisch, M. J. *et al.* Gaussian 16 Revision A.03 (2016).

[23] Fdez. Galvan, I. *et al.* Openmolcas: From source code to insight. *Journal of chemical theory and computation* **15**, 5925–5964 (2019).

[24] Ungur, L. & Chibotaru, L. F. Ab initio crystal field for lanthanides. *Chemistry–A European Journal* **23**, 3708–3718 (2017).

[25] Sarkar, A. & Rajaraman, G. Modulating magnetic anisotropy in Ln(iii) single-ion magnets using an external electric field. *Chem. Sci.* **11**, 10324–10330 (2020). URL http://dx.doi.org/10.1039/D0SC03982A.

[26] Wedge, C. J. *et al.* Chemical Engineering of Molecular Qubits. *Physical Review Letters* **108**, 107204 (2012). URL https://link.aps.org/doi/10.1103/PhysRevLett.108.107204.

[27] Kintzel, B. *et al.* Spin-electric coupling in a cobalt(II)-based spin triangle revealed by electric-field-modulated electron spin resonance spectroscopy. *Angewandte Chemie International Edition* **60**, 8832–8838 (2021). URL https://onlinelibrary.wiley.com/doi/abs/10.1002/anie.202017116. https://onlinelibrary.wiley.com/doi/pdf/10.1002/anie.202017116.

[28] Liu, Z. *et al.* Electric field manipulation enhanced by strong spin-orbit coupling: promoting rare-earth ions as qubits. *National Science Review* **7**, 1557–1563 (2020). URL https://academic.oup.com/nsr/article/7/10/1557/5863840.

[29] George, R. E., Edwards, J. P. & Ardavan, A. Coherent Spin Control by Electrical Manipulation of the Magnetic Anisotropy. *Physical Review Letters* **110**, 027601 (2013). URL https://link.aps.org/doi/10.1103/PhysRevLett.110.027601.

[30] Mi, X. *et al.* A coherent spin-photon interface in silicon. *Nature* **555**, 599–603 (2018). URL http://www.nature.com/doifinder/10.1038/nature25769.

Supplementary Information:
Quantum coherent spin-electric control in a molecular nanomagnet at clock transitions

Junjie Liu,[1,*] Jakub Mrozek,[1] Aman Ullah,[2] Yan Duan,[2] José J. Baldoví,[2]
Eugenio Coronado,[2] Alejandro Gaita-Ariño,[2,†] and Arzhang Ardavan[1,‡]

[1] *CAESR, Department of Physics, University of Oxford, The Clarendon Laboratory, Parks Road, Oxford OX1 3PU, UK*
[2] *Instituto de Ciencia Molecular (ICMol), Universitat de València, Paterna, Spain*

I. EXPERIMENTAL PULSE SEQUENCES

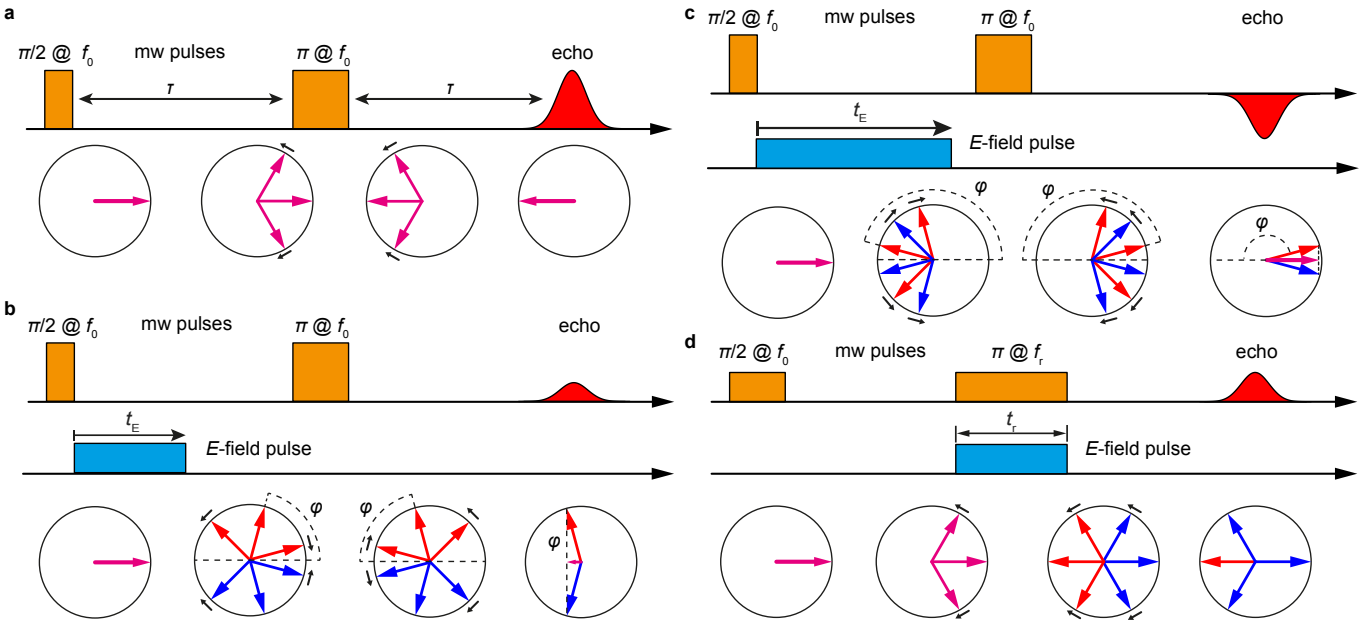

FIG. S1. Pulse sequences, together with the spin evolution schemes (in the xy plane of the Bloch sphere), depicting the formation of the spin echoes. In all sequences, the initial $\pi/2$ pulse rotates the spins parallel to the x axis. The blue and red arrows represent the spins for the crystallographically inequivalent HoW_{10} molecules related by inversion symmetry. The magenta arrows correspond to the summation of the red and blue arrows. **a**, Standard Hahn-echo sequence without any electric field. The evolutions of the blue and red spins are identical in the absence of an E-field pulse. The phase accumulation induced by static inhomogeneous (external or internal) magnetic fields in the first free evolution period is inverted by the π refocusing pulse. The spin echo is expected to form in the in-phase channel at $t = 2\tau$. **b**, An E-field pulse, applied immediately after the initial $\pi/2$ microwave pulse, increases (decreases) the precessing frequency for the red (blue) spins due to a linear spin-electric coupling (SEC) in HoW_{10} molecules. This leads to a $+\psi$ or $-\psi$ phase shift for the red and blue spins respectively, with $\psi = \delta f \times t_E$. The final echo is the summation of both red and blue spins and remains strictly in the in-phase channel, while its intensity (I) varies as $I \propto \cos(\delta f t_E)$. **c**, Upon further increasing the duration and/or amplitude of the E-field pulse, ψ increases, reversing the polarity of the spin echo. **d**, Electric-field-assisted spin selection. An E-field pulse is applied simultaneously with the refocusing π pulse, lifting the degeneracy in the ESR transitions of the two inversion-related subpopulations. When the frequency difference between the two subpopulations is larger than the excitation bandwidth of the π pulse, i.e. $|2\delta f| > 1/t_r$ (where t_r is the duration of the π pulse), only one subpopulation of the HoW_{10} spins (red arrows) is refocused by a π pulse with the frequency of $f_r = f_0 + \delta f$. The other subpopulation (blue arrows) does not form an echo because the phase accumulated owing to inhomogeneities is not refocused by the π pulse and instead accumulates monotonically throughout the pulse sequence. Therefore, the detected echo is comprised of only one subpopulation of the molecules.

* junjie.liu@physics.ox.ac.uk
† Alejandro.Gaita@uv.es
‡ arzhang.ardavan@physics.ox.ac.uk

II. MOLECULAR STRUCTURE FOR HoW_{10}

The Ho^{3+} ion is octa-coordinated by four oxygen atoms from each of the monolacunary Lindqvist moieties $[W_5O_{18}]^{6-}$ in a slightly distorted square antiprismatic geometry, providing an approximate D_{4d} symmetry for the Ho^{3+} centre (see Fig 1a in the main text). The deviation from the D_{4d} symmetry of the first coordination sphere of the Ho^{3+} centre can be described by the dihedral and the axial distortions. The dihedral distortion is the average of the absolute deviation of the skew angles θ from the ideal value (45° for D_{4d}). There are four possible skew angles which can be formed by the four independent pairs of O-Ho-O planes. The axial distortion is defined as the off-centre vertical displacement of the Ho^{3+} centre, expressed as $d = (h - h')/2$, where h and h' are the distances from the Ho^{3+} atom to the mean planes passing through the square bases of the antiprisms. The dihedral and the axial distortions for three different temperatures (100 K, 150 K and 200 K) are listed in Table S1. The single crystal structures of the same sample at three different temperatures (100 K, 150 K and 200 K) were determined and resolved in this work. CSD 2036358-2036360 contains the supplementary crystallographic data for this paper. These data can be obtained free of charge via `http://www.ccdc.cam.ac.uk/structures`, by emailing `data_request@ccdc.cam.ac.uk`, or by contacting The Cambridge Crystallographic Data Centre, 12 Union Road, Cambridge CB2 1EZ, UK; fax: +44 1223 336033.

On the basis of the crystal data and the optimized structure data, the quantification of the distortion is carried out by utilization of continuous shape measurement (CShMs) calculations using the SHAPE 2.1 software [S1, S2]. The values given by the Shape software are equal to 0, corresponding to the perfect polyhedron, and the larger value indicates the higher deviation from the ideal geometry. The obtained value of the eight-coordinated square antiprism (SAPR-8, D_{4d}) for HoW_{10} is well below 0.1, characteristic of systems that are only slightly distorted from the ideal symmetry of D_{4d}. This is true if we compare the crystallographic coordination sphere with SHAPE's internally defined D_{4d} polyhedron, which is defined with all vertices equidistant to the geometric centre and all edges of the same length ($S(Q, P) = 0.059$), and also if we compare the crystallographic coordination sphere with its D_{4d} idealization ($S(Q, P) = 0.038$).

TABLE S1. The dihedral and axial distortions (from the ideal D_{4d} symmetry) for the HoW_{10} molecules.

100 K		150 K		200 K	
θ (°)	$\lvert\theta - 45\rvert$ (°)	θ (°)	$\lvert\theta - 45\rvert$ (°)	θ (°)	$\lvert\theta - 45\rvert$ (°)
42.94(65)	2.06(65)	42.50(58)	2.50(58)	42.85(62)	2.15(62)
46.93(67)	1.93(67)	47.28(64)	2.28(64)	47.25(65)	2.25(65)
47.53(77)	2.53(77)	47.42(67)	2.42(67)	42.33(74)	2.33(74)
42.69(79)	2.31(79)	42.86(72)	2.14(72)	42.66(78)	2.34(78)
Off-centre distance (h and h')		Off-centre distance (h and h')		Off-centre distance (h and h')	
1.218(13) Å		1.273(11) Å		1.227(12) Å	
1.260(13) Å		1.223(12) Å		1.274(12) Å	
$d = (h - h')/2$		$d = (h - h')/2$		$d = (h - h')/2$	
0.021(13) Å		0.025(11) Å		0.024(12) Å	

III. *E*-FIELD INDUCED ESR FREQUENCY SHIFT DUE TO THE TETRAGONAL ANISOTROPY, THE HYPERFINE INTERACTION AND THE ELECTRONIC GYROMAGNETIC RATIO

At each of the experimental frequencies (9.15, 9.45 and 9.88 GHz), the E-field-induced shift in the ESR frequency (δf) is tuned by the changes in B_4^4, A and g_e differently. (The sixth order tetragonal transverse anisotropy, B_6^4, is also likely to be present, but it has the same effect on the clock transition as B_4^4 so we consider only B_4^4 here.) This can be understood from Fig. S2a, where the field dependence of the ESR transitions shows significant non-linear behaviour, indicating neither m_J nor m_I is a good quantum number in this field region and the eigenfunctions of the states associated with a given ESR transition are strongly affected by the magnetic field and/or the transition frequency. In order to parameterise the δf with the E-field-induced changes in the spin Hamiltonian parameters, we performed numerical simulations to analyse the experimental results.

We first consider δf at the clock transitions ($f = 9.15$ GHz). Fig. S3a-c show δf as a function of small variations in B_4^4, A and g_e, each varied by 10^{-4} of its value in the absence of an E-field. We also consider the effect of small errors in the magnetic field since the eigenstate of the HoW_{10} molecule varies with field rapidly around the clock transitions. At the exact clock transition field (H_{clock}), the ESR frequency is immune to small perturbations in the magnetic field (H). This is confirmed by the simulation in Fig. S3c, where δf is insensitive to changes in the g factor (δg) (the

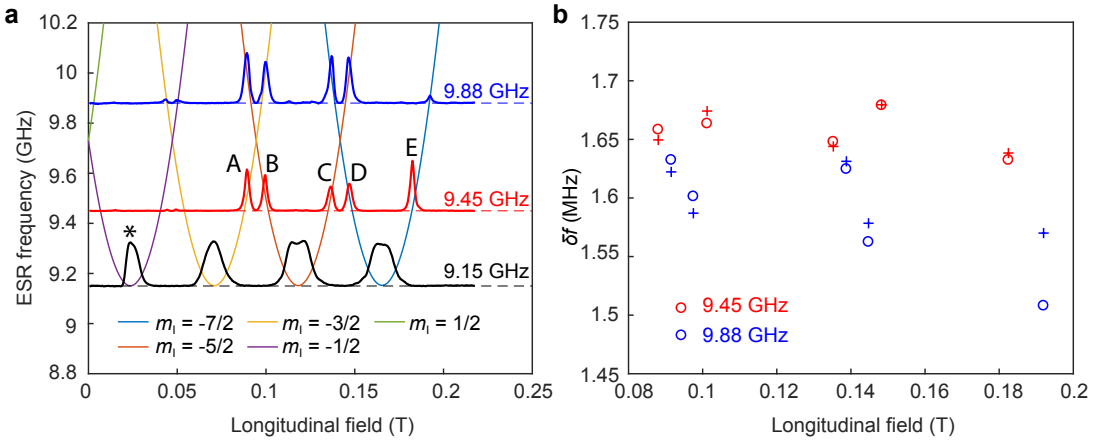

FIG. S2. (a) The ESR transition frequency versus the longitudinal component of the applied magnetic field ($= B_0 \cos 38°$). The ESR spectra are overlayed on top to illustrate the m_I and Δm_J value associated with different peaks. The experimental ($\circ$) and simulated ($+$) E-field induced ESR frequency shifts. The measurements were performed at the orientation with the strongest SEC and a fixed $V = 300$ V. The simulation is performed with the parameters in this section.

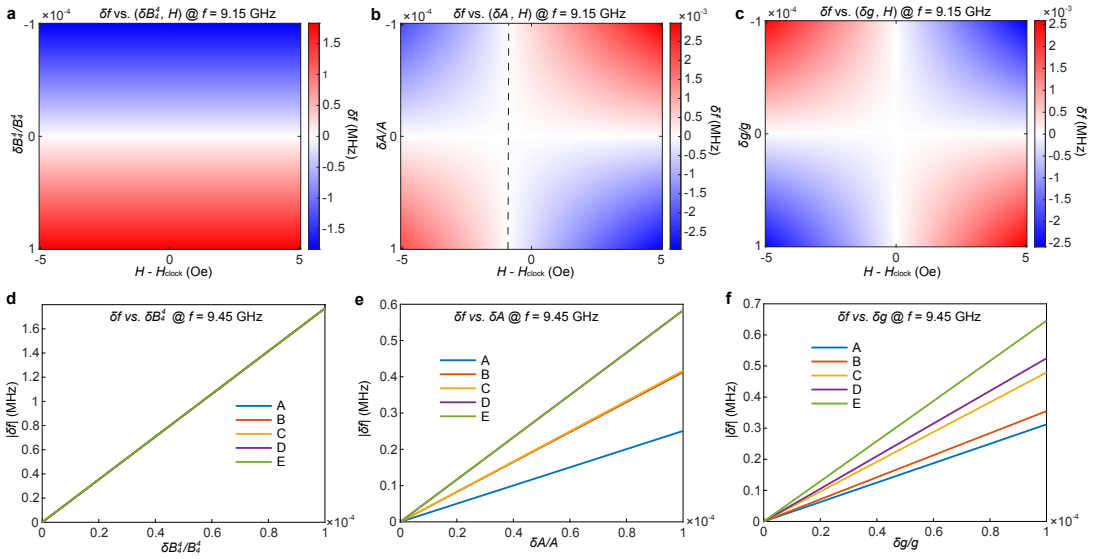

FIG. S3. (a)-(c) 2D colour plots showing the shift in the clock transition frequency (at $f = 9.15$ GHz) as a function of the longitudinal magnetic field and the spin Hamiltonian parameters B_4^4, A and g. The simulations were performed at the clock transition with the lowest magnetic field [labeled by * in Fig. S2(a)]. The parameters were varied by 10^{-4} of their $E = 0$ values (i.e. $|\delta B_4^4/B_4^4| \leq 10^{-4}$) to mimic the E-field induced small ESR shift, and the magnetic field was swept by 10 Oe around the clock transition field (H_{clock}) to evaluate the magnetic field dependence. Note the different scales for the colourbars. The frequency shifts induced by δA and δg are approximately 1000 times weaker than that caused by δB_4^4 at the clock transition frequency. (d)-(f) Magnetic field dependence for the shift in the ESR frequency (at $f = 9.45$ GHz) as a function of small changes inB_4^4, A and g. The frequency for all the ESR transitions [transitions labelled as A-E in Fig. S2(a)] exhibits linear dependence for small changes in the parameters. In addition, all A-E transitions show almost identical dependence on small changes in B_4^4, hence the five lines appear overlapping in Fig. S2(d).

magnetic field couples to the spins via $\mu_B \mu_0 HgJ$, therefore a change in g is equivalent to a change in H). Away from the clock transition field, δf shows a weak linear dependence on δg. A similar behaviour was found for A, even though the "clock field for hyperfine coupling" (the dashed vertical line in Fig. S3b) is slightly different from H_{clock} by about 1 Oe. Nevertheless, δf is only weakly affected by δA or δg around the clock transitions. Fig. S3b and c show that by varying $\delta A/A$ or $\delta g/g$ by up to 10^{-4}, δf is changed by less than 3×10^{-3} MHz, taking into account the possibility of errors in the applied magnetic field. In fact, in order to generate a δf of several MHz, a $\delta A/A$ ($\delta g/g$) $\approx 10\%$ is required, which is unlikely for the E-field applied in experiments. By contrast, a strong linear dependence for δB_4^4

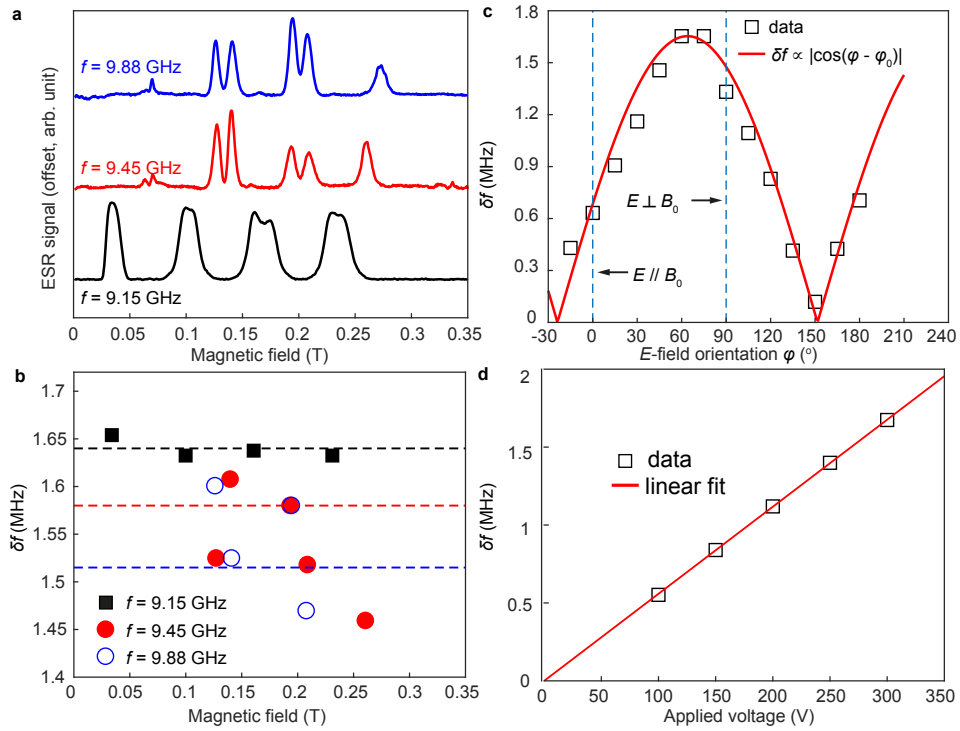

FIG. S4. Data recorded on Crystal B. (a) ESR spectra recorded at the CT frequency (9.15 GHz) and elevated frequencies (9.45 and 9.88 GHz). (b) shows the E-field effected measured on the corresponding transitions. The electric field is applied in the orientation with the strongest SEC. (c) Orientation dependence of the E-field induced frequency shift. The data were obtained with $f = 9.15$ GHz, $V = 300$ V and $B_0 = 0.0338$ T. (d) The frequency shift (recorded with $f = 9.15$ GHz and $B_0 = 0.0338$ T) versus the applied voltage showing a linear E-field coupling in Crystal B.

was found and this relation is insensitive to small errors in the magnetic field (Fig. S3a). In addition, the numerical simulation gives almost identical δf versus δB_4^4 relations for all four clock transitions (not shown), which is consistent with the experimental results that δf is magnetic field independent at the clock transition frequency (Fig.2d in the main text).

At elevated frequencies, δf is exhibits comparable linear dependence on δB_4^4, δA and δg. Fig. S3d-f show the simulation performed at $f = 9.45$ GHz for the different ESR transitions labeled in Fig S2a. While δf versus δB_4^4 is almost identical for all the five observed transitions (Fig. S3d), δf versus δA (and δf versus δg) varies significantly between them. By contrast, the difference between δf for A-E transitions at 9.45 GHz is less than 0.1 MHz in our experiments. Therefore, we attribute the E-field-induced effect mainly due a modification to the B_4^4 parameter, while the effects on A and g are much weaker, i.e. $\delta B_4^4/B_4^4 \gg \delta A/A$ or $\delta g/g$.

The best simulation of δf is shown in Fig. S2(b). This is obtained with $\delta B_4^4 = 8.8 \times 10^{-3}$ MHz, $\delta g_e = 1.87 \times 10^{-5}$ and $\delta A = 1.54 \times 10^{-2}$ MHz. As shown in Fig. S2(b), these parameters simulate the fluctuations in δf well, except at the highest field resonance observed for $f = 9.88$ GHz. This deviation is likely to be due to the misalignment in the B_0 field, which leads to a nontrivial contribution to the ESR transition frequencies due to the transverse component of the magnetic field. Thus the tetragonal transverse anisotropy is the spin Hamiltonian term most strongly coupled to the E-field, with $\delta B_4^4/B_4^4 = 9.3 \times 10^{-5}$, compared to $\delta g_e/g_e = 1.6 \times 10^{-5}$ and $\delta A/A = 1.8 \times 10^{-5}$, for an applied voltage of 300 V.

IV. DATA FROM THE SECOND CRYSTAL

We repeated the experiments on a different crystal, namely Crystal B. Crystal B was picked from a different batch of crystals grown under the same conditions. The ESR spectra [Fig. S4(a)] for Crystal B suggest its easy axis is aligned approximately 45° away from the B_0 field.

As shown in Fig. S4, the data recorded on Crystal B are similar to those presented in the main text. In particular, the maximum SEC parameter (11.2 Hz/V m^{-1}) is virtually identical to the value reported in the main text (11.4 Hz/V m^{-1}). On the other hand, the orientation dependence for Crystal B is offset by approximately 90° compared

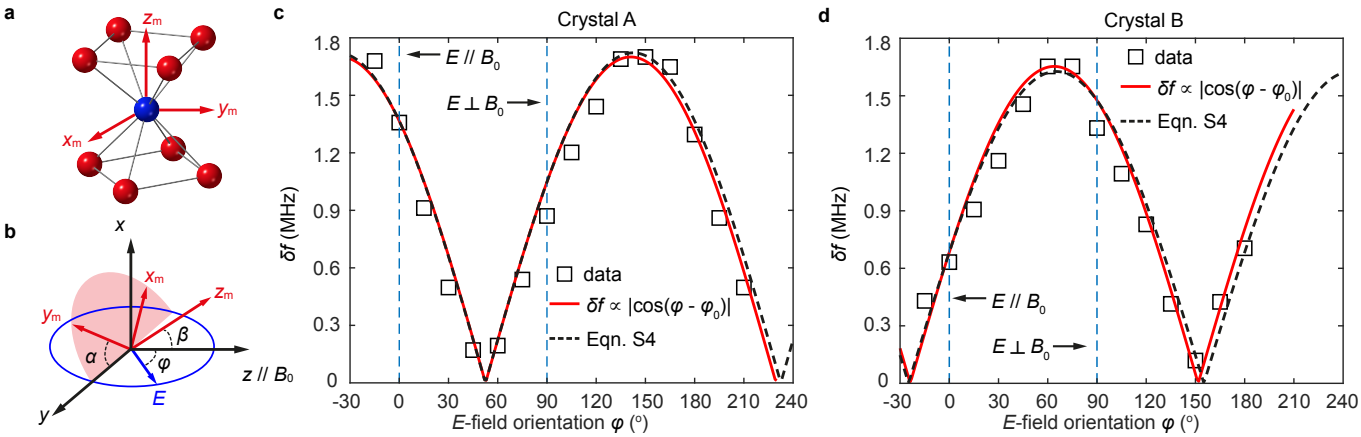

FIG. S5. (a) The molecular frame $(x_\mathrm{m}, y_\mathrm{m}, z_\mathrm{m})$ and (b) the conversion between the molecular and the laboratory frame (x, y and z). The molecular easy axis, z_m, lies in the laboratory $x-z$ plane. β corresponds to the misalignment between the molecular easy axis and B_0 whereas α is unknown. φ indicates the orientation of the E-field in the $y-z$ plane. (c) and (d) are the orientation dependence data for Crystals A and B, respectively. The dashed lines are the simulations performed with Eqn. S4 and the parameters included in this section.

to the result in the main text. This is due to the crystallographic packing of the HoW_{10} crystals, where the molecular easy axis does not align with any unit cell axes or crystal facets, as well as the limitation that we can only perform a single-axis rotation on the sample. Therefore, it is challenging to control the orientation of the sample in the experiments. We analyse this offset in the next section. Nevertheless, δf also follows $\delta f \propto |\cos(\varphi - \varphi_0)|$ in Crystal B with the maximum/minimum of the SEC occurring shifted away from the molecular magnetic axes. Both observations are in agreement with the results on Crystal A described in the main text.

V. ORIENTATION DEPENDENCE OF THE E-FIELD INDUCED FREQUENCY SHIFT

In the E-field orientation dependence experiments, the applied electric field is rotated within the laboratory y–z plane such that $\mathbf{E} = (0, E\sin\varphi, E\cos\varphi)$. As described in the main text, the frequency shifts for the two inversion-related HoW_{10} subpopulations are opposite. Therefore, the observed $\delta f \propto |\cos(\varphi - \varphi_0)|$ relation implies that for a given HoW_{10} molecule,

$$\begin{aligned}\delta f &= \text{const} \times E\cos(\varphi - \varphi_0) \\ &= \text{const} \times (\cos\varphi_0 E\cos\varphi + \sin\varphi_0 E\sin\varphi) \\ &= \mathbf{A}_l^\mathrm{E} \cdot \mathbf{E},\end{aligned} \tag{S1}$$

where $\mathbf{A}_l^\mathrm{E}$ is the vector depicting the SEC for HoW_{10} molecules is in the laboratory frame. $\mathbf{A}_l^\mathrm{E}$ is different for Crystals A and B due to the difference in the crystal alignments. In the molecular frame, we define the local coordination x_m, y_m and z_m, with z_m being parallel to the molecular easy axis (Fig. S5a). In this local frame, the SEC coupling $\mathbf{A}_m^\mathrm{E} = (A_{m,x}, A_{m,y}, A_{m,z})$. We note $\mathbf{A}_m^\mathrm{E}$ is also affected by the ESR frequency. However, for the low-field CT measured in the orientation dependence experiments, δf is only affected by the change in the tetragonal anisotropy, i.e. δB_4^4, and insensitive to B_0 misalignment (as shown in the previous section); therefore, $\mathbf{A}_m^\mathrm{E}$ is identical for both crystals. Importantly, $\mathbf{A}_m^\mathrm{E}$ does not coincide with the molecular easy axis, i.e. $A_{m,x} \neq 0$ (and/or $A_{y,m} \neq 0$). This would imply that $\delta f = 0$ when the E-field is applied within the molecular hard plane ($\varphi = 90°$), which contradicts with the experimental results.

The conversion between the molecular and the laboratory frame is shown in Fig. S5b and can be described by the rotation matrix R_m^l where

$$R_m^l = \begin{pmatrix} \cos\alpha\cos\beta & -\sin\alpha & -\cos\alpha\sin\beta \\ \sin\alpha\cos\beta & \cos\alpha & -\sin\alpha\sin\beta \\ \sin\beta & 0 & \cos\beta \end{pmatrix} \tag{S2}$$

The E-field induced frequency shift:

$$\begin{aligned}\delta f =& \mathbf{A}_m^{\mathrm{E}} \cdot R_m^l \cdot \mathbf{E} \\ =& E(A_{m,y}\cos\alpha - A_{m,x}\sin\alpha)\sin\varphi + E(A_{m,z}\cos\beta - A_{m,x}\cos\alpha\sin\beta - A_{m,y}\sin\alpha\sin\beta)\cos\varphi.\end{aligned} \tag{S3}$$

Without loss of generality, we can choose x_{m} such that $\mathbf{A}_m^{\mathrm{E}}$ lies in the x_{m}–z_{m} plane, i.e., $A_{m,x} \neq 0$ and $A_{m,y} = 0$. Eqn. S3 can be further simplified so that

$$\delta f = -EA_{m,x}\sin\alpha\sin\varphi + E(A_{m,z}\cos\beta - A_{m,x}\cos\alpha\sin\beta)\cos\varphi, \tag{S4}$$

where $\beta = 38°$ and $45°$ for crystal A and B, respectively. On the other hand, the angle α *cannot* be directly extrapolated from the ESR spectra. It is the different combinations of α and β leads to the non-identical orientation dependence for Crystals A and B, even when the electric field is applied parallel to B_0.

The parameters in Eqn. S4 can be calculated using the orientation dependence data. We consider the E-field induced frequency shift at $\varphi = 0$ and $90°$ for Crystals A and B. This gives

$$\begin{aligned}\delta f_{\mathrm{A}}(\varphi = 0) =& E(A_{m,z}\cos\beta_{\mathrm{A}} - A_{m,x}\cos\alpha_{\mathrm{A}}\sin\beta_{\mathrm{A}}) \\ \delta f_{\mathrm{A}}(\varphi = 90°) =& -EA_{m,x}\sin\alpha_{\mathrm{A}} \\ \delta f_{\mathrm{B}}(\varphi = 0) =& E(A_{m,z}\cos\beta_{\mathrm{B}} - A_{m,x}\cos\alpha_{\mathrm{B}}\sin\beta_{\mathrm{B}}) \\ \delta f_{\mathrm{B}}(\varphi = 90°) =& -EA_{m,x}\sin\alpha_{\mathrm{B}},\end{aligned} \tag{S5}$$

where the subscript A and B correspond to Crystal A and B, respectively. $\beta_{\mathrm{A}} = 38°$ and $\beta_{\mathrm{B}} = 45°$. $E = 1.5\times10^5$ V/m.

It is worth noting that the sign for $\delta f(\varphi)$ cannot be determined from the experiments. However, based on the orientation dependence, $\delta f_{\mathrm{A}}(\varphi = 0)$ and $\delta f_{\mathrm{A}}(\varphi = 90°)$ should have opposite sign while $\delta f_{\mathrm{B}}(\varphi = 0)$ and $\delta f_{\mathrm{B}}(\varphi = 90°)$ should have the same sign. The exact sign for $\delta f(\varphi)$ is not important as it can be altered by a trivial inversion operation.

The orientation dependence for both crystals can be explained best (Fig. S5c and d) with $A_{m,x} = 9.8$ Hz/(V m^{-1}), $A_{m,z} = 6.1$ Hz/(V m^{-1}), $\alpha_{\mathrm{A}} = -45°$ and $\alpha_{\mathrm{B}} = 88°$. The analysis shows that the principal SEC axis for HoW_{10} is significantly tilted ($\approx 58°$) away from the molecular easy axis.

VI. E-FIELD ENABLED SELECTIVE SPIN EXCITATION DATA

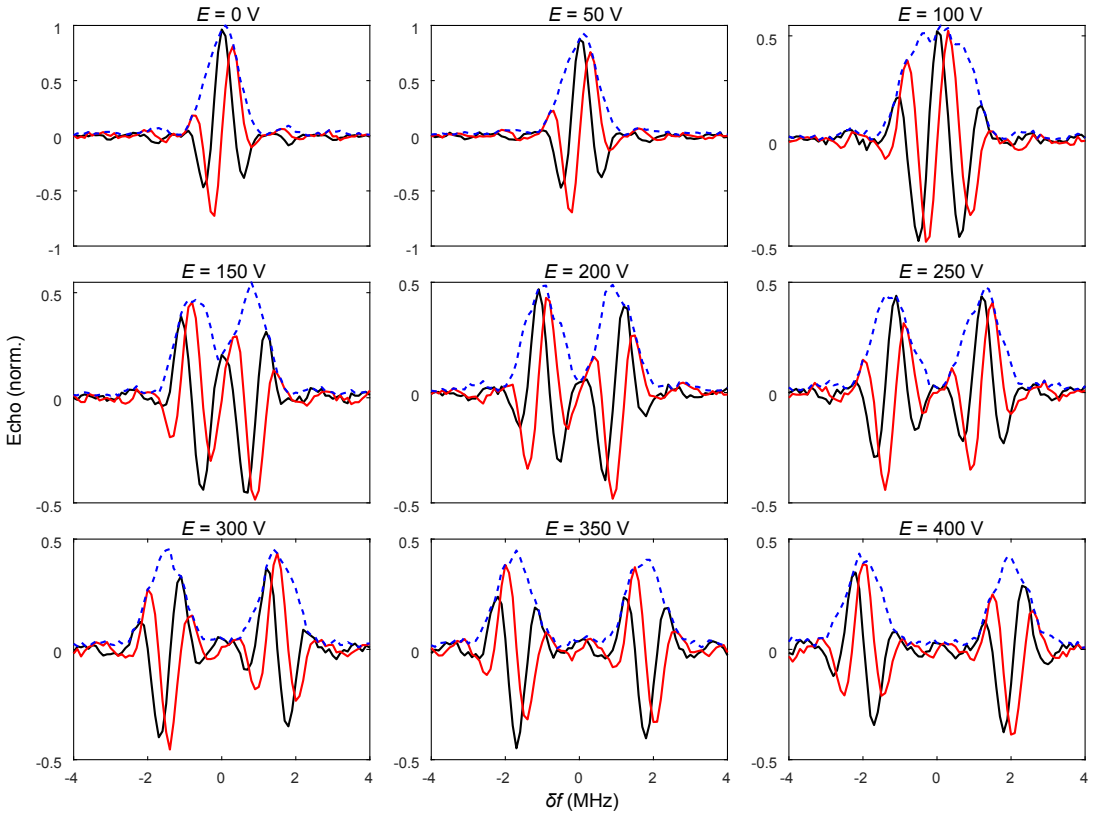

FIG. S6. The spin echo signals versus the frequency shift of the refocusing pulse in the E-field-enabled selective spin excitation experiment (Fig. 3 in the main text). Each subplot corresponds to the data recorded with a different applied voltage. The black and red solid lines represent the in-phase and quadrature components respectively and the blue dashed lines represent the absolute magnitude of the spin echo.

VII. ELECTRIC FIELD EXCITATION FOR SPIN TRANSITIONS

The experiments in this work demonstrate non-resonant coherent spin control with an E-field [S3]. However, it is also possible to excite a spin transition with a high-frequency resonant E-field. Here we discuss the E-field strength required for such operations in HoW_{10}. We consider the SEC for the tetragonal anisotropy since it is the dominant contribution in the vicinity of the clock transitions (CT). The application of an oscillating electric field $\boldsymbol{E}(t) = E\cos\omega t$ gives rise to a time dependent term $\delta B_4^4 \hat{O}_4^4 \cos\omega t$, where δB_4^4 is determined by the amplitude and orientation of the applied E-field. This could drive a transition between two spin states, namely $|n\rangle$ and $|m\rangle$, with a transition rate, i.e. Rabi frequency f_{Rabi}, given by

$$hf_{\text{Rabi}} = |\delta B_4^4 \langle m| \hat{O}_4^4 |n\rangle|. \tag{S6}$$

where h is Planck's constant.

Fig. S7 shows the transition rates for the ground $m_J = \pm 4$ multiplet. Exactly at the CT field, the states are eigenfunctions of $\hat{O}_4^4$ and the transition rate vanishes (Fig. S7b). Away from the CT field, an oscillating $B_4^4\hat{O}_4^4$ term connects states with the same nuclear spin projection m_I, allowing an oscillating E-field to drive a spin transition directly. Here we consider a 9.88 GHz E-field, at which frequency a $T_2 \approx 1\mu$s was observed at 5 K for samples with 0.1% HoW_{10} concentration.

With the maximum observed SEC coupling of $\delta B_4^4/h = 5.9 \times 10^{-2}$ Hz/Vm^{-1}, the E-field Rabi rate (Eqn. S6) at 9.88 GHz is estimated to be 1.4 Hz/Vm^{-1}. Hence, an E-field of 10^6 V/m = 1 mV/nm is required in order to achieve coherent spin control, $f_{\text{Rabi}} < T_2^{-1}$. Such fields are accessible in nanogaps. In fact, it is possible to generate this

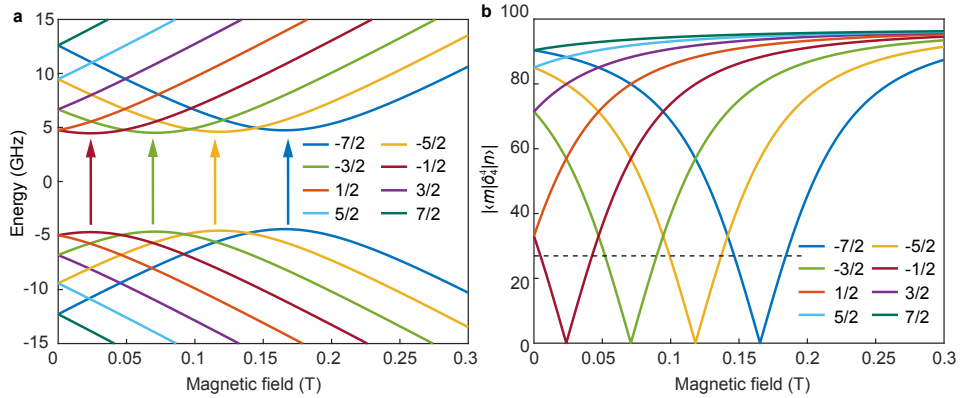

FIG. S7. **a**, The Zeeman energy diagram of the ground $m_J = \pm 4$ multiplet for HoW_{10} with the magnetic field applied parallel to the magnetic axial direction. The states are sorted according to the nuclear spin projection m_I. The CTs are indicated by the vertical arrows. **b**, The transition rate for the E-field induced spin excitations, $|\langle m|\,\hat{O}_4^4\,|n\rangle|$, between states with the same m_I. The horizontal dashed line indicates the transition rate for $f = 9.88$ GHz.

field in certain macroscopic 3D resonators, for instance, a loop-gap resonator [S4], allowing, in principle, ensemble experiments on single-crystal samples.

VIII. COMPUTATIONAL DETAILS

A. Electronic and vibrational structure

The time-independent electronic structure was computed using the multireference Complete Active Self-Consistent Field Spin-Orbit (CASSCF-SO) method as implemented in the OpenMOLCAS program package (version 18.09) [S5]. The molecular geometry was extracted from the single-crystal X-ray structure and was fully optimized at density functional theory (DFT) level (*vide infra*). In addition, the electronic structure of the molecular geometry with no prior optimization was calculated. Scalar relativistic effects were taken into account with the Douglas–Kroll–Hess transformation using the relativistically contracted atomic natural orbital ANO-RCC basis set with VDZP quality for all atoms. The active space consisted of 10 electrons on the 7 f-orbitals of Ho^{3+} ion. The molecular orbitals were optimized at the CASSCF level in a state-average (SA) over 35 quintets of the ground state term ($L = 6$ for Ho^{3+}). The wave functions obtained at CASSCF were then mixed by spin-orbit coupling by means of the RASSI approach. The combined effect of the crystal field and the spin orbit coupling were computed using SINGLE-ANISO module [S6].

The structural optimization of the crystallographic coordinates in vacuum and the vibrational modes calculations were carried out at DFT level using the Gaussian16 package in its revision A.03 [S7]. The vibrational frequency calculations were carried out using both the fully optimized structure and the X-ray crystal structure with no optimization. The PBE0 hybrid exchange-correlation functional was used for both optimization and frequency calculations in combination with Stuttgart RSC ANO basis set with effective core potential (ECP) for the Ho^{3+} cation. CRENBL basis set have been used for W with corresponding ECP potential and 6-31G(d,p) basis set had been used for oxygen. An 'ultra-fine' integration grid and 'very tight' SCF convergence criterion were applied. Dispersion effects were taken into account using the empirical GD3BJ dispersion correction.

The crystalline environment of the polyanion has an effect in its electric dipole. We estimated this effect by recalculating the electric dipole for all the distorted geometries in an embedding consisting in a crystalline fragment. We chose this fragment to consist of 11 units of HoW_{10} molecule, $11\times$ ($Na_9[Ho(W_5O_{18})_2]\cdot 35H_2O$). The charge analysis of the environment atoms was performed in Gaussian16 using MKUFF uses the Merz-Kollman-Singh approximate charges to fit the electrostatic potential of the molecule. The electronic energy for the central HoW_{10} molecule in the presence of the environment as point-charges was stabilized at same level of DFT as optimization and vibrational frequencies calculations (the input/output files are provided as SI files).

B. General methodology

Let us start by laying out the effective Hamiltonian we will use to model the spin-electric coupling in HoW_{10}. $\hat{H}_{\text{eff}}$ is the sum of (i) a time-independent crystal-field Hamiltonian $\hat{H}_{\text{CF}}(J)$, which is only a function of the equilibrium molecular geometry acting on the ground multiplet J and (ii) the perturbation $\hat{H}_{\text{CF}}(J, Q_{\text{eff}}(V))$ resulting from the collective distortion coordinate $Q_{\text{eff}}(V)$ which is in itself a function of the externally applied electric voltage V:

$$\hat{H}_{\text{eff}} = \hat{H}_{\text{CF}}(J) + \hat{H}_{\text{CF}}(J, Q_{\text{eff}}(V)) \tag{S7}$$

In order to estimate the effect of the molecular distortion caused by the external electric field, we chose to decompose such a distortion in the geometrical basis of the vibrational modes. Since we are operating in the regime of very small distortions (small fractions of an angstrom), the total effect of every vibrational normal mode will be additive in a very good approximation. Thus, we proceeded considering that, being $3N-6$ the number of vibrational modes (n) in nonlinear molecules of N atoms and that, for a given applied voltage, the effective distortion $\vec{Q}_{\text{eff}}$ can be written as the additive effect of all of the displacements corresponding to n vibrational modes as defined in Eqn. S8:

$$\vec{Q}_{\text{eff}}(V) = \sum_n Q_{(\text{eff},n)}(V) = Q_{(\text{eff},1)}(V) + Q_{(\text{eff},2)}(V) + \ldots + Q_{(\text{eff},3N-6)}(V) \tag{S8}$$

where $Q_{(\text{eff},n)}(V)$ is the distortion attained by a normal mode n at a given applied potential V, which can be further expressed as displacement vector of normal mode as in Eqn. S9:

$$\vec{Q}_{(\text{eff},n)} = v_n(V) \begin{pmatrix} q_{x,n} \\ q_{y,n} \\ q_{z,n} \end{pmatrix} \tag{S9}$$

Thus, the total spin-electric coupling can be effectively estimated if one is able to relate the external voltage with the induced molecular distortions, and these with the perturbation $\hat{H}_{\text{CF}}(J, Q_{\text{eff}}(V))$. In the subsequent sections, we detail, step by step, the general methodology that we employed to estimate the spin-electric coupling in this molecular spin qubit.

C. Step 1: Derivation of the relation between molecular distortion and electric field

To model the evolution of the tunneling splitting caused by an electrical field, we first had to correlate the distortion of atomic coordinates and the E-field. For this we considered the fact that the perturbation caused by applied E-field is necessarily at the cost of molecular distortions from a near-equilibrium structure. In particular, a central assumption in our methodology is that the rise in potential energy due to the displacement of the atomic positions – in the form of a harmonic oscillator – is exactly matched by the stabilization of the potential energy due to the change in the molecular electric dipole in presence of an external electric field.

For technical reasons, we could not calculate the effect of an external E-field in terms of molecular distortions directly. Instead, we calculated this indirectly using a set of distorted structures following the vibrational modes of HoW_{10} as input and estimated the change in electrical dipole associated to each distortion. Then, the electrical field that is required to achieve a given distortion was estimated by computing the harmonic potential energy and dipole moment at a given point. This was carried out at different points along the vibrational path by using the following Eqn. S10:

$$U_n = -\Delta p E \cos\rho \tag{S10}$$

where U_n is the harmonic potential energy, Δp is the increase in the (molecular) electric dipole moment at any given distortion compared with the value in the absence of distortions and ρ is the angle between the external electric field E and the dipole moment. Except where we were explicitly calculating the angular dependence, we worked assuming that the electric field E was applied exactly in the direction of the molecular electric dipole p in the equilibrium geometry. Moreover, since experimentally we worked in the regime of very small distortions, we assumed that the change in the electric dipole Δp can be properly approximated at all experimentally relevant voltages by a change in its modulus $|\Delta p|$ and we neglected the effect of any change in the angle $\Delta\rho$ caused by the distortion:

$$E = -\frac{U_n}{|\Delta p|} \tag{S11}$$

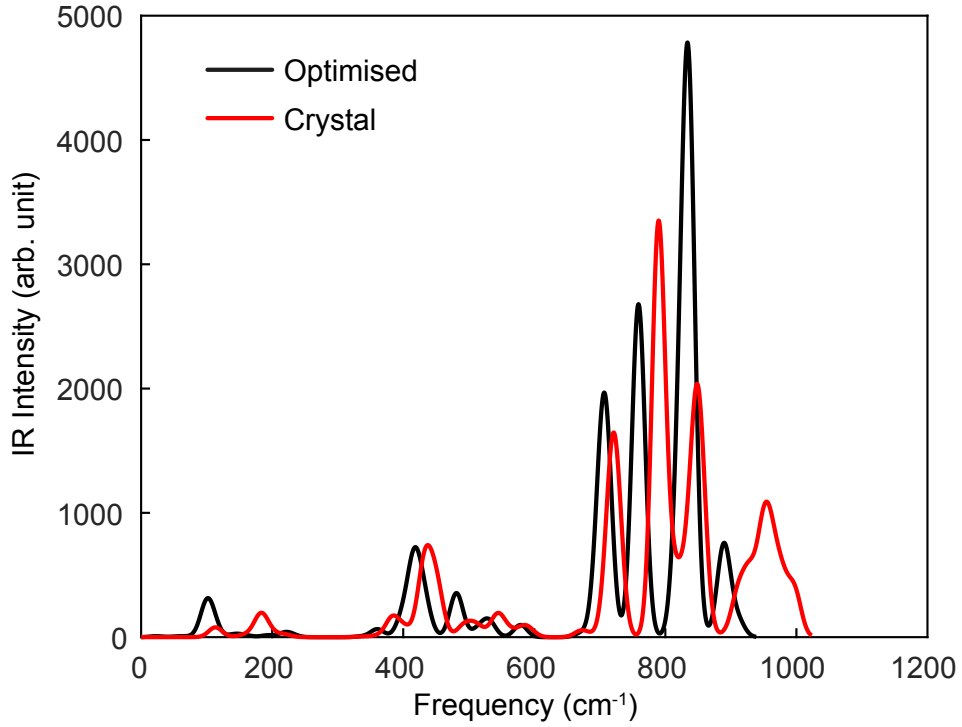

FIG. S8. Harmonic vibrational frequencies for HoW_{10}, IR intensities with Gaussian-convoluted FWHM of 10 cm^{-1} for optimized structure (black) and for crystal structure (red).

Following this approach, firstly we calculated the potential energy for a given vibrational mode n by using the classical potential energy Eqn. S12:

$$U_n = \frac{1}{2} k_n Q_n^2 \tag{S12}$$

where k_n is the force constant of mode n and Q_n is a displacement along the vibrational coordinate $\vec{Q}_n$ of mode n. We choose the origin of potential energy $U_n = 0$ at the equilibrium coordinates $\vec{Q}_{\text{eq}}$ where $v_n = 0$.

We then defined for each normal mode a series of displacement vectors of increasing moduli, given by

$$\vec{Q}_n = v_n \begin{pmatrix} q_{n,x} \\ q_{n,y} \\ q_{n,z} \end{pmatrix} \tag{S13}$$

with the corresponding series distorted atomic coordinates being given by $\vec{Q}_{\text{dist}} = \vec{Q}_{\text{eq}} + \vec{Q}_n$ where 'v_n' is a scalar multiplier which defines the step or modulus of the displacement between consecutive distorted geometries following a given vibrational path. The value of v_n was chosen to be large enough to produce consistent values of the electric dipole, since distortions corresponding to the experimentally realistic perturbations are very small and we found that the results were heavily affected by numerical errors in the Gaussian output.

At this point, the procedure is straightforward. The external electric field E is the result of an externally applied voltage V_{ext}, with the relation between the two magnitudes being given by the distance $d = 0.002$ m between two plates:

$$E = V_{\text{ext}}/d \tag{S14}$$

At each of the same set of distorted coordinates where we calculated the elastic distortion energy as detailed above, we also computed the dipole moment at the DFT level. The external voltage V resulting in an electric field that achieves an energy match between the molecular distortion energy Q cost and the electric potential energy stabilization is the external voltage required for precisely that degree of molecular distortion $Q_{(\text{eff},n)}(V)$. Again, note that the useful information we can get for changes in the electrical dipole is limited by numerical noise for distortions below a certain threshold; we therefore needed to apply relatively large distortions (larger than 0.02 Å). The electric field

needed to achieve any given molecular distortion is given by combining Eqn. S14 and S12, i.e. the electric field where the stabilization due to the change in the electric dipole potential energy is exactly enough to compensate the cost in terms of elastic spring energy. Due to the above mentioned technical limitations, the theoretically obtained distortions are relatively large, corresponding to electric fields that are approximately 5 orders of magnitude above the experimentally available E-field. As discussed below, we performed a quadratic interpolation to the limit of small distortions to access the experimentally relevant electric fields.

D. Step 2: DFT calculation of vibrational spectrum and electric dipoles

The obtained frequencies for optimized- and crystal-geometry are provided in Table S2 and S3 respectively, and also plotted in Fig. S8. From Fig. S8, we observed the vibrational frequency for optimized geometry is redshifted with respect to crystal geometry. Further, we analysed that the IR-active mode in both cases; they present similar displacement patterns. (Output files are provided for analysis of displacement pattern.) This gives us confidence to use the optimized geometry for further analysis.

TABLE S2: Frequencies (cm^{-1}) computed at the DFT level for relaxed-geometry, resultant displacement d_{Ho} (Å), IR/k and effective normalized displacement $Q_{(\mathrm{eff},n)}$ for each normal mode (n).

Mode (n)	Frequency (cm^{-1})	d_{Ho} (Å)	IR/k $\left(\frac{\mathrm{km.mol^{-1}}}{\mathrm{mDyne.Å^{-1}}}\right)$	$\lvert Q_{(\mathrm{eff},n)}\rvert$ (300V) ($10^{-5}\times$Å)
1	8.62	0.008	5.22	6.6608
2	17.94	0.022	200.69	7.4497
3	18.43	0.004	102.42	10.7773
4	24.33	0.072	493.41	3.6713
5	29.97	0.046	0.68	0.0995
6	43.22	0.169	5.39	0.6575
7	54.02	0.501	25.52	1.1618
8	58.39	0.304	13.89	0.8202
9	67.12	0.302	11.34	1.0228
10	70.95	0.433	16.91	0.4642
11	99.61	0.481	611.40	0.0389
12	106.52	0.070	0.54	0.0221
13	106.78	0.112	6.77	0.0461
14	107.26	0.089	0.58	0.4116
15	108.76	0.223	470.90	0.0632
16	114.68	0.028	0.28	0.0410
17	114.71	0.036	1.44	0.1167
18	140.11	0.054	4.85	0.1636
19	140.76	0.021	1.24	0.0325
20	141.19	0.027	1.21	0.1342
21	142.11	0.007	0.04	0.0886
22	143.98	0.126	24.44	0.0272
23	144.75	0.032	0.01	0.0311
24	157.60	0.018	5.09	0.1569
25	158.17	0.002	0.00	0.0017
26	159.14	0.007	0.78	0.0161
27	159.88	0.047	11.82	0.0915
28	160.56	0.038	10.16	0.3349
29	161.30	0.001	0.01	0.0428
30	167.76	0.002	0.01	0.0116
31	167.77	0.002	0.01	0.0104
32	184.62	0.006	0.11	0.0521
33	184.73	0.005	0.06	0.0656
34	193.02	0.052	28.11	0.0565
35	202.14	0.012	0.02	0.0964
36	216.40	0.001	1.60	0.1246
37	216.89	0.003	2.39	0.1896
38	218.12	0.001	0.62	0.0411
39	218.13	0.002	0.85	0.0340
40	218.22	0.002	0.41	0.0240
41	218.24	0.003	0.82	0.0312
42	219.96	0.006	26.18	0.2854

43	220.00	0.006	29.47	0.2012
44	220.07	0.004	5.10	0.0094
45	220.47	0.001	0.19	0.0295
46	223.18	0.002	2.87	0.0788
47	224.41	0.005	0.69	0.0797
48	230.85	0.000	10.81	0.1760
49	231.24	0.001	11.22	0.1345
50	231.75	0.000	0.39	0.0506
51	232.10	0.001	0.52	0.0578
52	235.13	0.000	0.10	0.0101
53	235.33	0.000	0.01	0.0082
54	257.49	0.001	0.00	0.0079
55	257.49	0.001	0.00	0.0075
56	289.55	0.001	0.00	0.0165
57	291.07	0.001	0.00	0.0096
58	329.19	0.002	0.04	0.0120
59	329.25	0.002	0.05	0.0083
60	337.26	0.015	2.36	0.1373
61	337.36	0.007	0.65	0.0500
62	337.40	0.015	2.31	0.0362
63	337.72	0.007	0.49	0.0084
64	351.19	0.011	0.08	0.0187
65	354.95	0.000	0.03	0.0372
66	355.21	0.002	0.22	0.0298
67	359.02	0.016	15.44	0.1602
68	360.26	0.022	24.79	0.2391
69	363.49	0.016	9.62	0.0729
70	399.03	0.002	69.09	0.0082
71	399.78	0.003	19.05	0.0852
72	399.80	0.002	6.49	0.0649
73	404.19	0.005	0.34	0.0049
74	414.55	0.004	28.49	0.1228
75	414.92	0.003	25.14	0.2106
76	416.67	0.008	110.35	0.3117
77	416.90	0.008	106.28	0.3797
78	417.53	0.004	23.52	0.0566
79	417.69	0.004	26.77	0.1741
80	429.95	0.010	120.59	0.0066
81	431.15	0.006	5.73	0.0902
82	435.19	0.003	0.16	0.0161
83	436.31	0.009	1.00	0.0101
84	436.72	0.006	28.09	0.0001
85	437.91	0.008	6.11	0.0356
86	479.05	0.001	0.79	0.0230
87	479.34	0.001	0.61	0.0335
88	480.96	0.006	74.70	0.2299
89	481.29	0.007	76.78	0.2741
90	489.34	0.000	1.05	0.0093
91	489.38	0.001	1.35	0.0323
92	514.29	0.010	23.83	0.0278
93	515.09	0.001	0.32	0.0087
94	515.25	0.001	0.20	0.0101
95	516.21	0.001	0.03	0.0237
96	520.31	0.002	0.24	0.0191
97	521.09	0.002	0.16	0.0324
98	528.07	0.003	4.88	0.0163
99	529.22	0.003	0.17	0.0216
100	530.46	0.002	36.75	0.0084
101	531.81	0.002	4.44	0.0169
102	535.59	0.002	0.23	0.0237
103	536.21	0.002	1.91	0.0277
104	554.98	0.000	0.02	0.0075
105	555.04	0.000	0.02	0.0073
106	578.43	0.000	7.88	0.0580

107	579.04	0.000	7.57	0.0588
108	579.13	0.000	7.80	0.0548
109	579.49	0.000	6.37	0.0650
110	671.58	0.001	6.78	0.0042
111	671.94	0.001	0.14	0.0022
112	697.89	0.013	49.15	0.1883
113	698.02	0.014	52.43	0.0739
114	708.22	0.020	160.98	0.3199
115	708.89	0.020	165.23	0.1571
116	759.02	0.005	449.21	0.0015
117	766.97	0.000	0.20	0.0127
118	819.87	0.005	123.01	0.0038
119	825.83	0.000	2.13	0.0242
120	827.39	0.003	20.35	0.0296
121	829.18	0.001	21.79	0.1111
122	829.87	0.003	16.64	0.0612
123	832.87	0.001	3.85	0.0286
124	835.00	0.006	207.17	0.2909
125	835.25	0.005	194.49	0.1041
126	835.94	0.004	172.35	0.1051
127	885.27	0.001	13.24	0.0278
128	886.09	0.001	1.52	0.0375
129	886.14	0.001	1.99	0.0009
130	887.81	0.000	0.44	0.0294
131	888.08	0.001	0.92	0.0111
132	889.51	0.001	47.50	0.1326
133	891.28	0.002	31.47	0.0579
134	910.99	0.005	15.48	0.0066
135	913.68	0.001	0.01	0.0117

TABLE S3: Frequencies (cm^{-1}) computed at the DFT level for crystal-geometry, resultant displacement d_{Ho} (Å), IR/k and effective normalized displacement $Q_{(\mathrm{eff},n)}$ for each normal mode (n).

Mode (n)	Frequency (cm^{-1})	d_{Ho} (Å)	IR/k $\left(\frac{\mathrm{km.mol^{-1}}}{\mathrm{mDyne.Å^{-1}}}\right)$	$\left\|Q_{(\mathrm{eff},n)}\right\|$ (300V) ($10^{-5}\times$Å)
1	-28.79	0.003	0.07	1.5949
2	-15.56	0.165	1.94	5.9928
3	-9.24	0.167	4.84	57.8133
4	50.80	0.005	0.02	0.0312
5	58.62	0.015	1.53	0.2590
6	59.16	0.017	0.98	0.2560
7	89.61	0.014	0.45	0.0228
8	93.12	0.029	0.24	0.3186
9	107.58	0.355	1.20	0.1921
10	108.82	0.382	0.52	0.0847
11	112.86	0.385	165.61	0.0132
12	116.50	0.180	17.97	0.0609
13	120.99	0.079	4.18	0.0342
14	123.78	0.067	2.63	0.1512
15	124.79	0.112	2.42	0.1503
16	127.15	0.064	0.20	0.2250
17	129.14	0.090	5.90	0.0433
18	132.29	0.033	0.43	0.1431
19	140.81	0.022	0.39	0.1992
20	146.08	0.044	0.62	0.1236
21	146.48	0.037	0.10	0.0358
22	148.52	0.034	0.09	0.0097
23	155.17	0.201	4.19	0.1612
24	156.35	0.193	2.73	0.0976
25	157.65	0.236	10.48	0.1913
26	159.42	0.093	0.71	0.1014
27	159.87	0.097	3.47	0.0738

28	161.39	0.056	0.50	0.0596
29	162.42	0.022	0.47	0.0567
30	163.17	0.089	2.36	0.0599
31	165.24	0.065	2.98	0.0173
32	175.82	0.075	67.22	0.0555
33	179.44	0.041	30.81	0.1789
34	179.75	0.067	43.34	0.0521
35	182.99	0.101	145.85	0.1236
36	184.26	0.106	160.25	0.3455
37	186.40	0.012	27.90	0.4980
38	187.52	0.022	15.49	0.0194
39	192.14	0.035	21.37	0.0162
40	192.96	0.006	26.53	0.3005
41	196.98	0.025	19.73	0.0464
42	199.59	0.017	5.92	0.0470
43	201.54	0.038	7.69	0.1226
44	202.02	0.007	6.97	0.1228
45	203.38	0.026	6.43	0.0787
46	210.95	0.010	0.45	0.0160
47	212.77	0.011	2.75	0.0731
48	215.70	0.012	13.18	0.1985
49	217.91	0.009	11.12	0.0727
50	221.22	0.028	7.40	0.0169
51	223.05	0.007	1.72	0.0656
52	223.32	0.003	0.20	0.0418
53	224.14	0.004	0.27	0.0590
54	248.64	0.002	0.06	0.0078
55	251.92	0.002	0.05	0.0332
56	286.74	0.001	0.05	0.0036
57	298.58	0.002	0.03	0.0087
58	334.12	0.007	2.02	0.0810
59	336.97	0.006	1.14	0.0110
60	340.45	0.005	0.92	0.0008
61	342.15	0.004	0.39	0.0243
62	350.79	0.005	0.46	0.0120
63	357.49	0.021	3.17	0.0321
64	359.96	0.019	3.38	0.0089
65	368.65	0.006	1.59	0.0488
66	370.48	0.011	2.79	0.1127
67	371.56	0.008	1.56	0.0184
68	382.80	0.050	48.78	0.2183
69	384.12	0.049	52.70	0.3082
70	400.93	0.016	42.42	0.0409
71	408.80	0.002	0.08	0.0269
72	410.29	0.001	0.53	0.0145
73	413.73	0.006	3.38	0.0250
74	429.15	0.007	95.17	0.3867
75	430.56	0.006	33.47	0.0083
76	432.50	0.008	63.87	0.1998
77	433.66	0.004	19.89	0.0801
78	436.61	0.013	115.18	0.0278
79	438.18	0.002	10.90	0.0676
80	441.65	0.006	2.78	0.0513
81	446.08	0.008	42.41	0.2545
82	447.02	0.003	7.58	0.0313
83	448.84	0.006	44.60	0.0859
84	452.42	0.004	49.01	0.2869
85	454.07	0.004	52.70	0.1299
86	483.17	0.001	0.13	0.0010
87	485.31	0.002	1.73	0.0224
88	489.00	0.004	6.81	0.0902
89	491.33	0.007	15.24	0.1141
90	494.43	0.005	6.10	0.0415
91	498.30	0.005	13.19	0.0674

92	509.57	0.008	29.06	0.0556
93	514.27	0.002	2.15	0.0366
94	517.25	0.001	1.78	0.0261
95	519.36	0.005	6.09	0.0886
96	522.59	0.002	1.27	0.0266
97	531.27	0.002	0.77	0.0276
98	538.87	0.002	14.62	0.0416
99	539.62	0.002	0.24	0.0076
100	544.50	0.002	32.07	0.0330
101	547.37	0.002	17.43	0.0345
102	553.72	0.002	1.18	0.0129
103	557.35	0.003	3.37	0.0172
104	560.95	0.001	3.89	0.0681
105	565.08	0.002	7.64	0.0844
106	581.27	0.001	13.83	0.0126
107	587.13	0.001	8.14	0.0209
108	592.71	0.001	7.74	0.0688
109	597.88	0.002	2.25	0.0341
110	668.48	0.004	6.06	0.0727
111	676.61	0.002	7.25	0.0456
112	703.54	0.006	9.21	0.0764
113	715.01	0.010	34.60	0.0654
114	718.59	0.021	169.76	0.2701
115	726.41	0.019	135.88	0.2049
116	789.41	0.002	514.36	0.0146
117	808.11	0.001	62.81	0.0116
118	823.42	0.002	43.22	0.0679
119	830.73	0.001	20.25	0.0899
120	841.04	0.002	10.40	0.0124
121	843.98	0.001	34.60	0.0775
122	845.61	0.001	99.00	0.0847
123	851.20	0.002	106.04	0.2365
124	856.37	0.001	53.05	0.0818
125	891.65	0.001	2.67	0.0135
126	910.48	0.000	38.95	0.0074
127	925.61	0.002	18.83	0.0877
128	929.00	0.002	34.85	0.0863
129	946.44	0.002	22.95	0.0603
130	948.48	0.002	44.47	0.0875
131	957.48	0.002	44.90	0.0717
132	965.21	0.003	33.26	0.0441
133	978.33	0.002	38.16	0.1191
134	992.95	0.005	8.23	0.0045
135	998.23	0.002	28.26	0.0549

E. Environment

Each central HoW_{10} is surrounded by a layer of 18 HoW_{10} units. The distances between the central Ho to the neighbouring Ho atoms are listed in the Table S4. We chose to surround the central HoW_{10} unit with 10 neighbours, because there is an abrupt increase in distance (of 3.235 Å) from the 10^{th} neighbour to the 11^{th}; see Fig. S9.

For the calculation of electrical dipole moment, we replaced the environment with point-charges, as shown in Fig. S10. The electric dipole was calculated in the presence of the environment not only at the optimized geometry but also at a series of distorted geometries from the equilibrium optimized geometry, following the displacement vectors of each vibrational mode. In each calculation we extracted the electric dipole of HoW_{10}. Fig. S11 and S12 show the results for the optimized geometry. The analogous calculations are represented in Fig. S15 and S16 for the crystal geometry.

For each distorted structure, the combination of the calculated force constant and the change in electric dipole compared with the undistorted structure allows us, employing the equations indicated above, to estimate the external electric field that would be needed to achieve said distortion. Thus, we can associate an E-field to every degree of

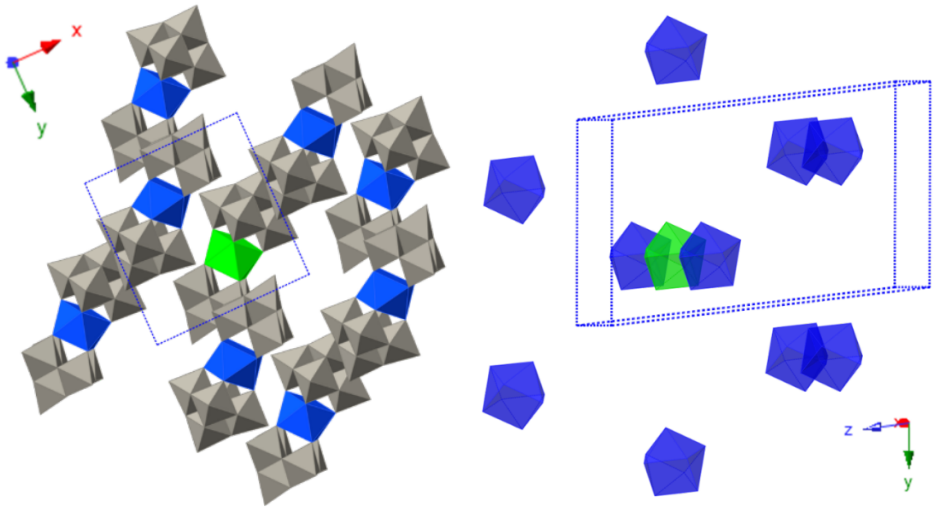

FIG. S9. Left: Packing diagram of anionic HoW_{10} component in the crystal structure viewed along the *c*-axis using polyhedral representation. Blue (surrounding 10 Ho atoms) and green (one central Ho atom) square antiprism, HoO_8 units; Grey octahedra, WO_6. For clarity, sodium ions and water molecules are not shown. Right: Packing diagram of Ho atoms in the crystal structure using polyhedral representation. Blue (surrounding 10 Ho atoms) and green (one central Ho atom) square antiprism HoO_8 units.

distortion of each normal mode of the optimized structure shown in Fig. S13 and S14. The analogous calculations for the crystal geometry are represented in Fig. S17 and S18.

TABLE S4. The Ho-Ho distances for a given HoW_{10} molecule and its 18 nearest neighbours

n^{th} neighbour	Ho-Ho distance (Å)	n^{th} neighbour	Ho-Ho distance (Å)
1	11.212	10	13.443
2	12.478	11	16.678
3	12.734	12	17.25
4	12.734	13	18.069
5	12.93	14	18.069
6	13.074	15	18.431
7	13.074	16	18.431
8	13.239	17	18.434
9	13.422	18	18.6

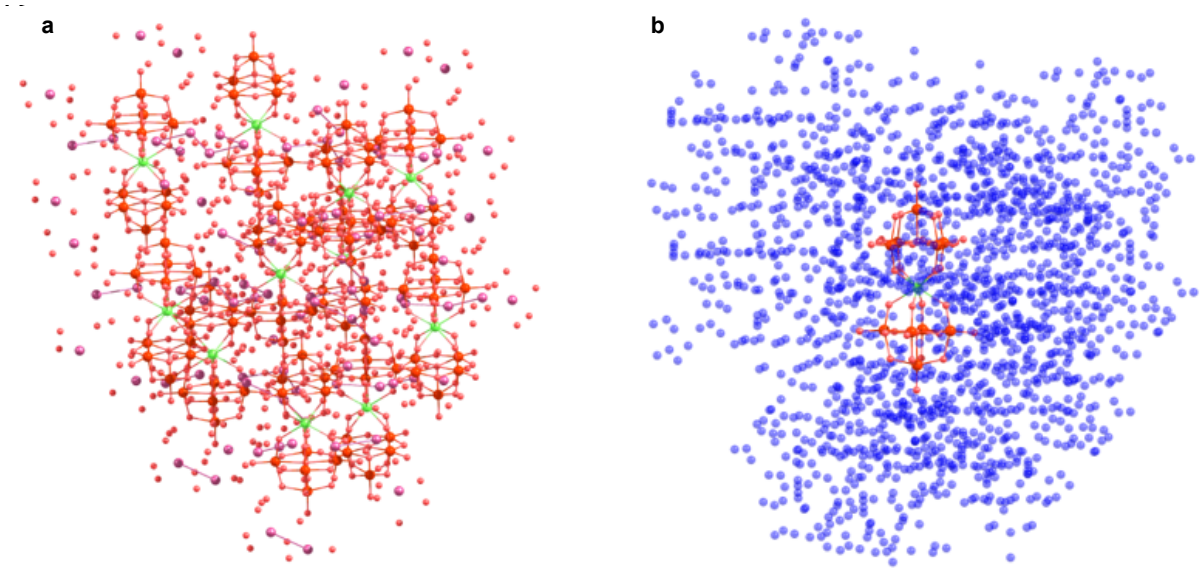

FIG. S10. (a) The fragment of $11\times(Na_9[Ho(W_5O_{18})_2]\cdot 35H_2O)$ on their crystallographic coordinates as employed to provide an environment to the central polyoxometalate; for clarity, hydrogen atoms are not shown. (b) Simplified system to model the electrostatic potential offered by environment, where all external entities $10\times Na_9[Ho(W_5O_{18})_2]\cdot 35H_2O$ as well as the nine Na^+ countercations and thirty-five crystallization water molecules of the central polyoxometalate are replaced by point charges (blue).

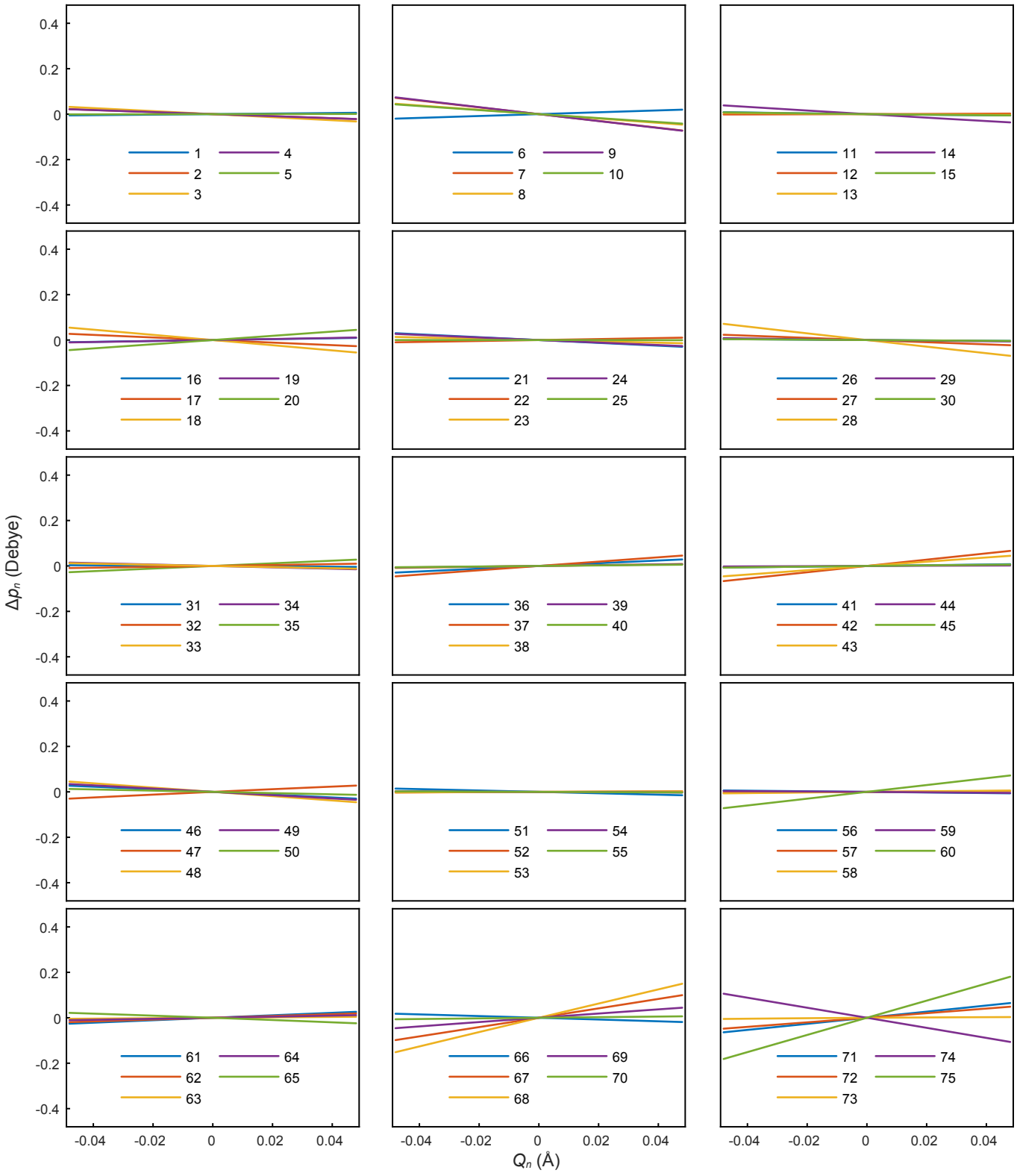

FIG. S11. Change in dipole moment Δp_n for normal modes 1-75 for the optimized structure.

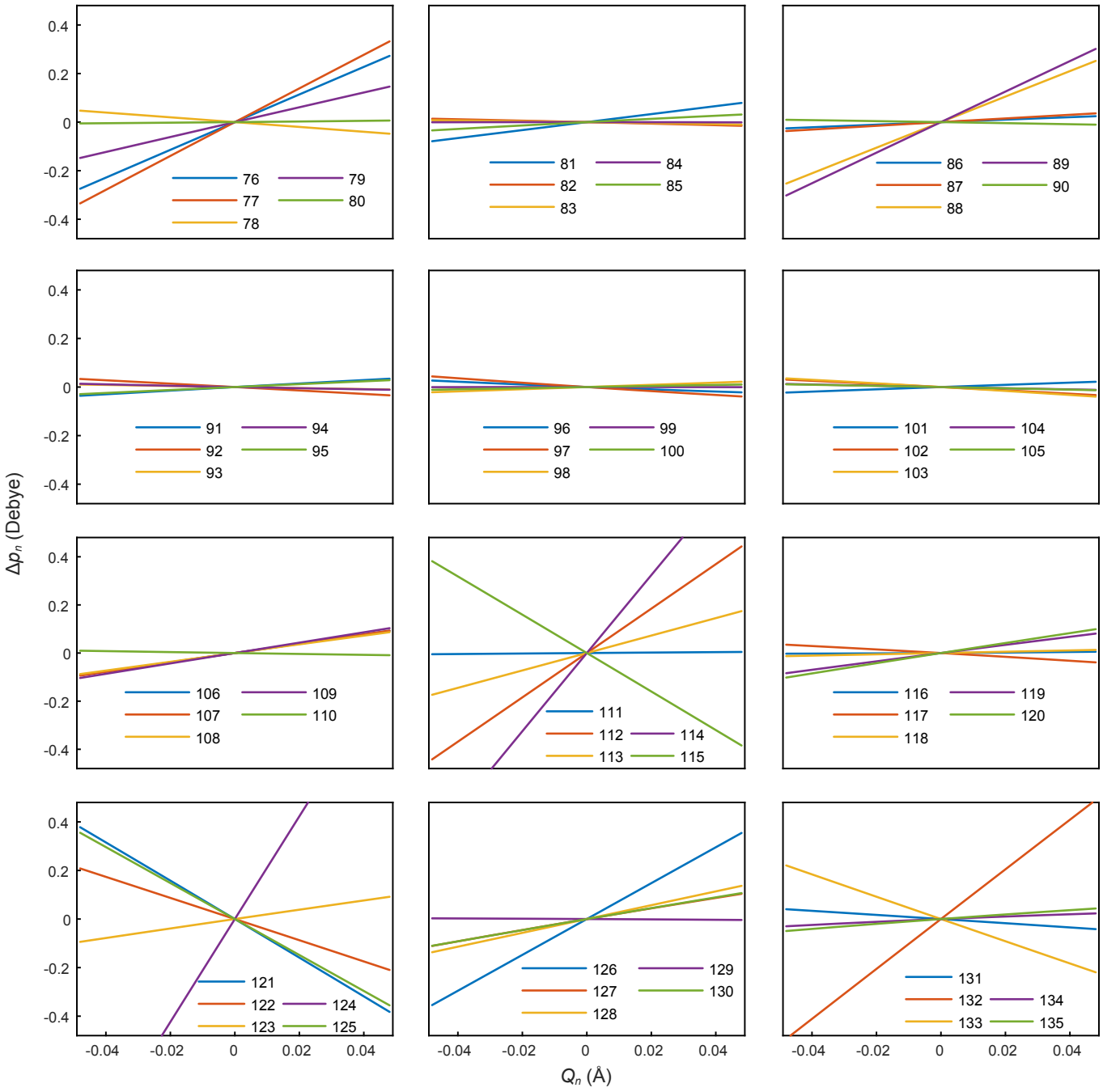

FIG. S12. Change in dipole moment Δp_n for normal modes 76-135 for the optimized structure.

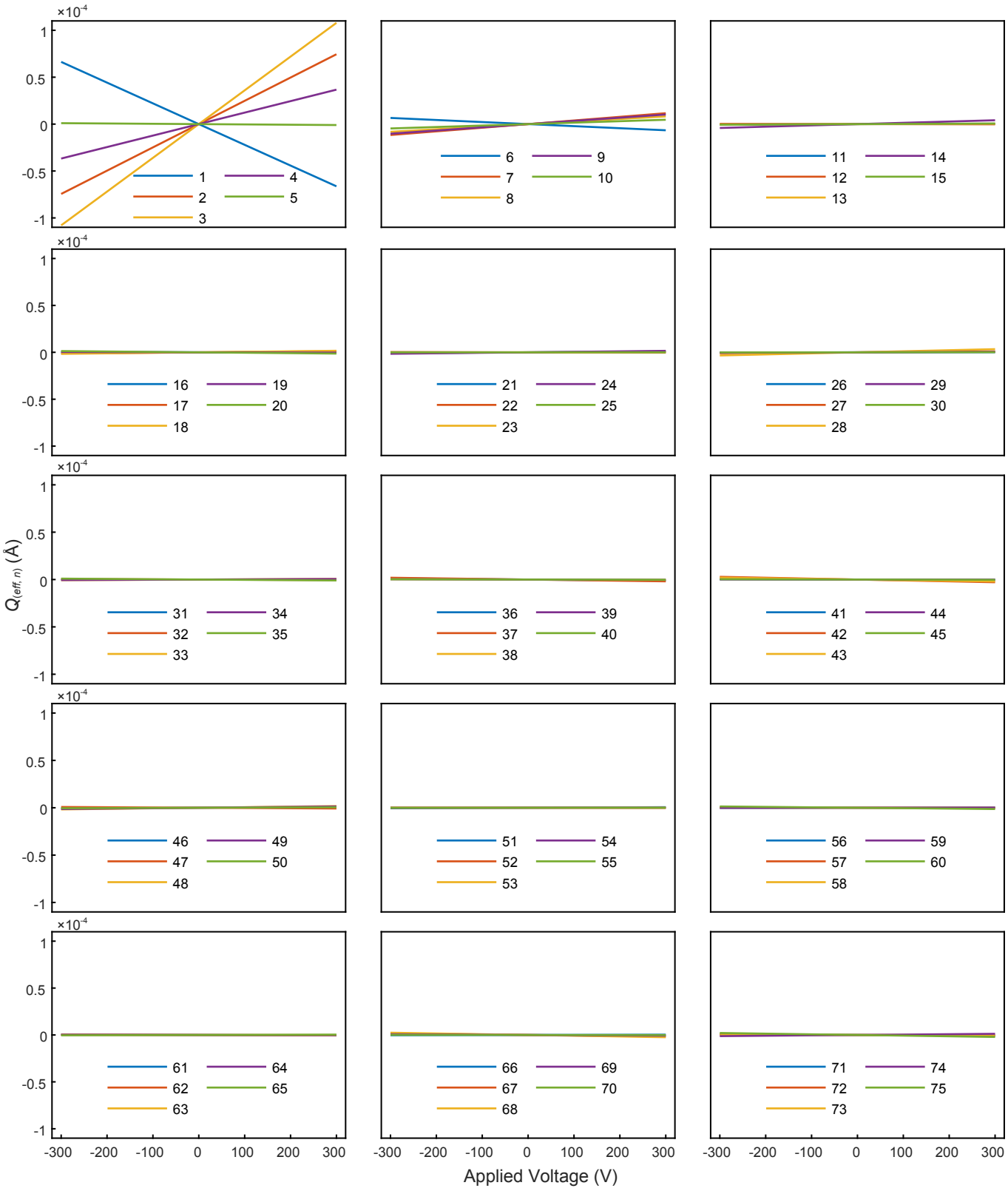

FIG. S13. Effective distortion attained by normal modes 1-75 of the optimized structure at applied voltages.

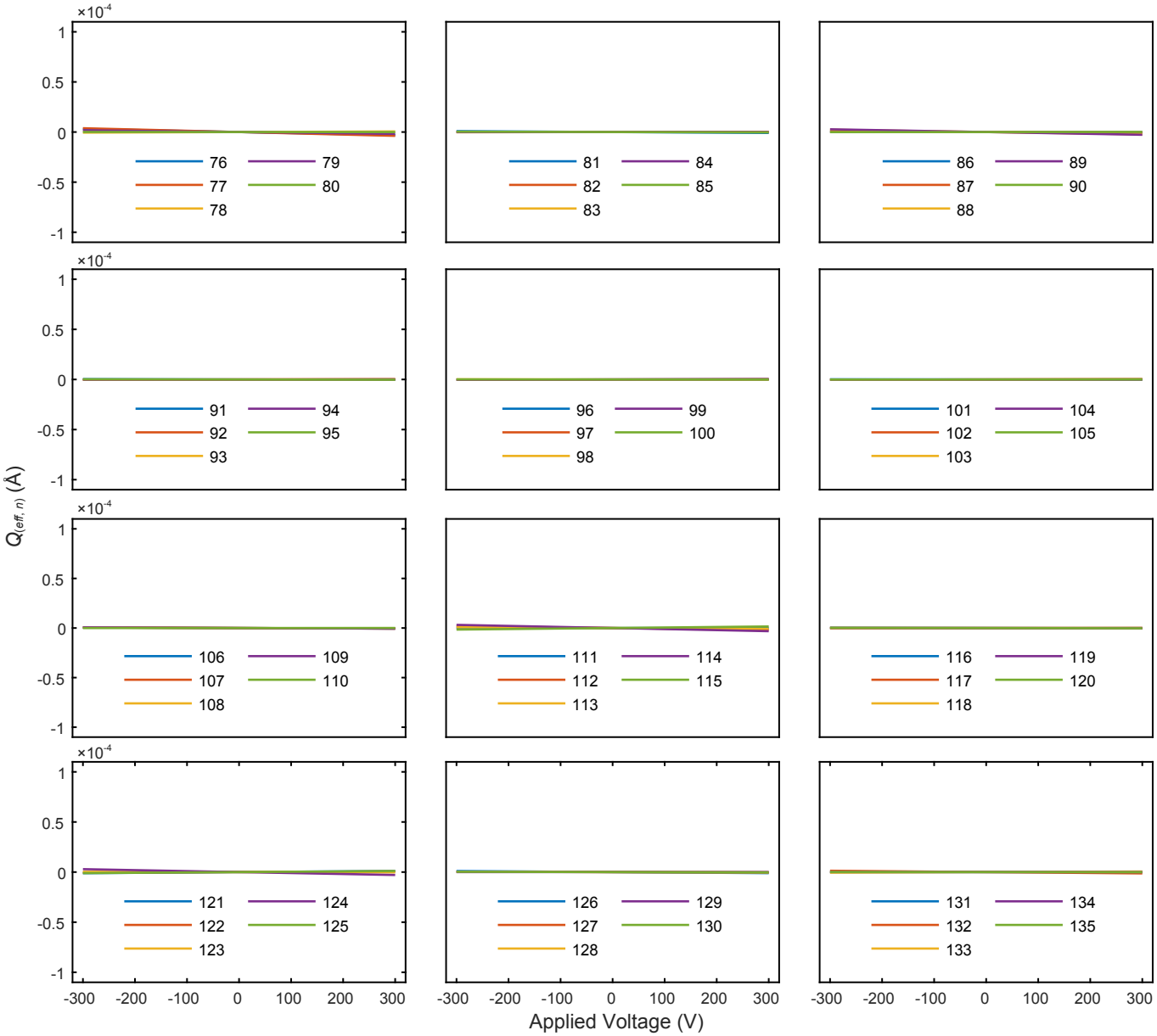

FIG. S14. Effective distortion attained by normal modes 76-135 of the optimized structure at applied voltages.

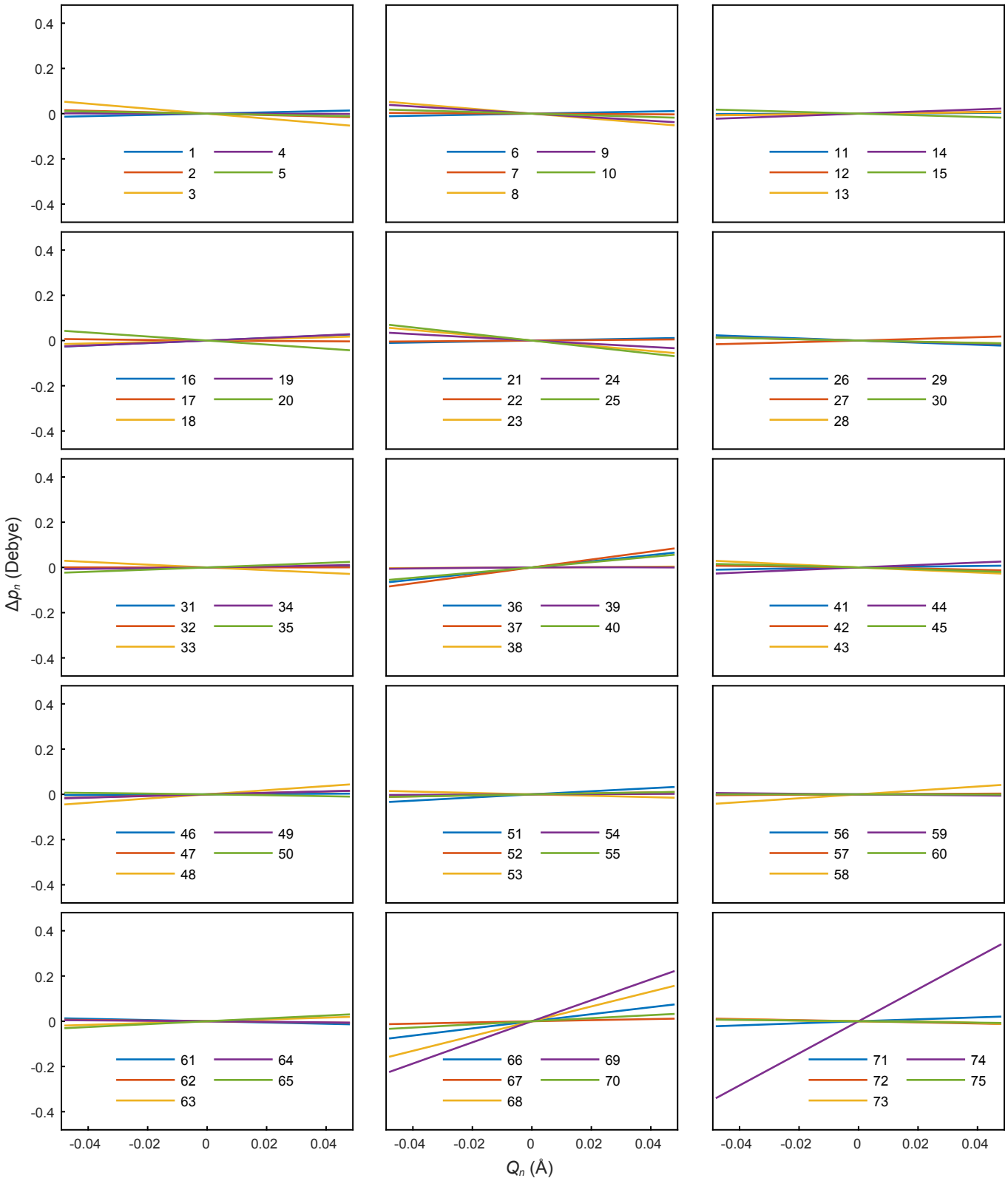

FIG. S15. Change in dipole moment Δp_n for normal modes 1-75 for the crystal structure.

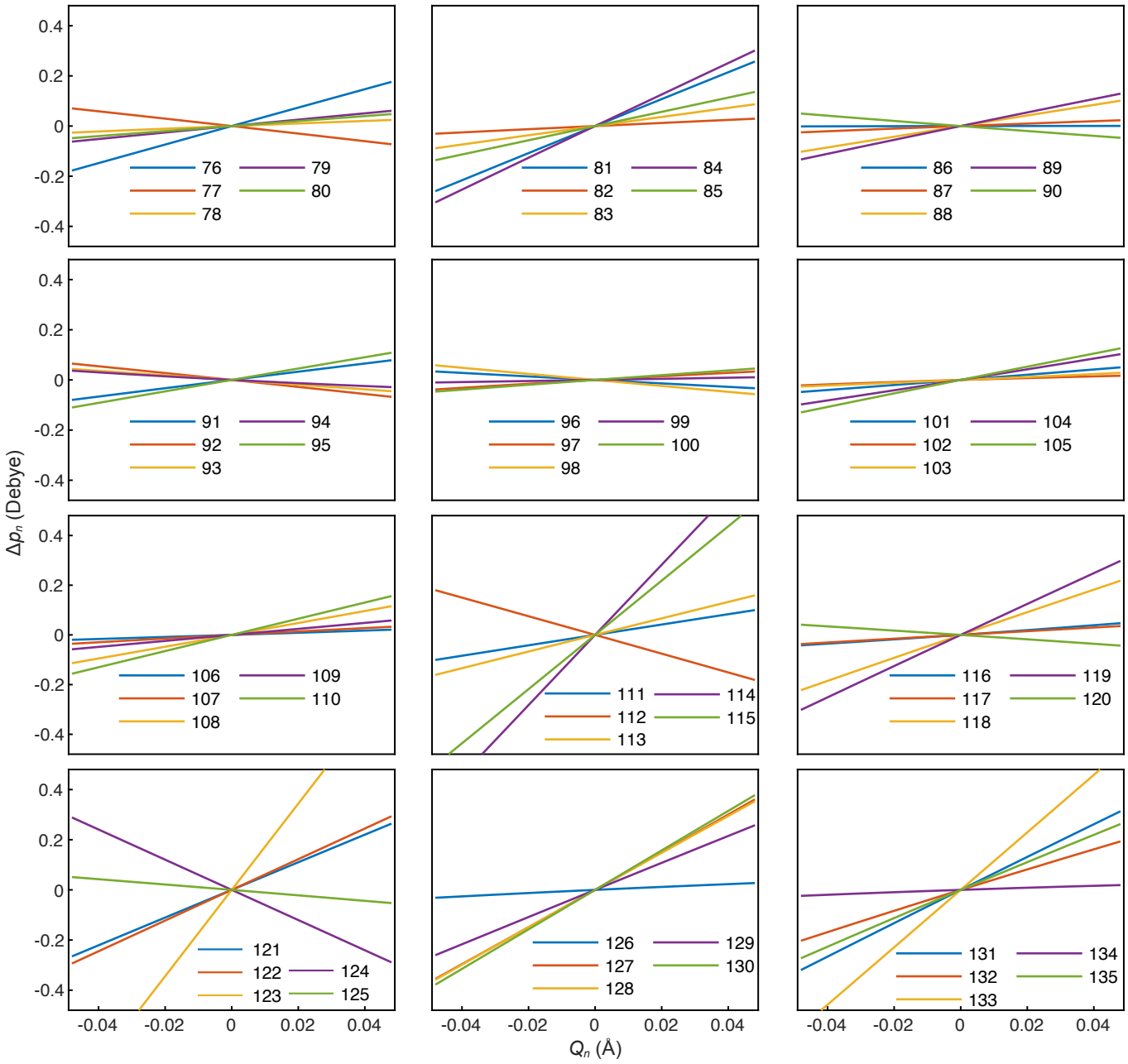

FIG. S16. Change in dipole moment Δp_n for normal modes 76-135 for the crystal structure.

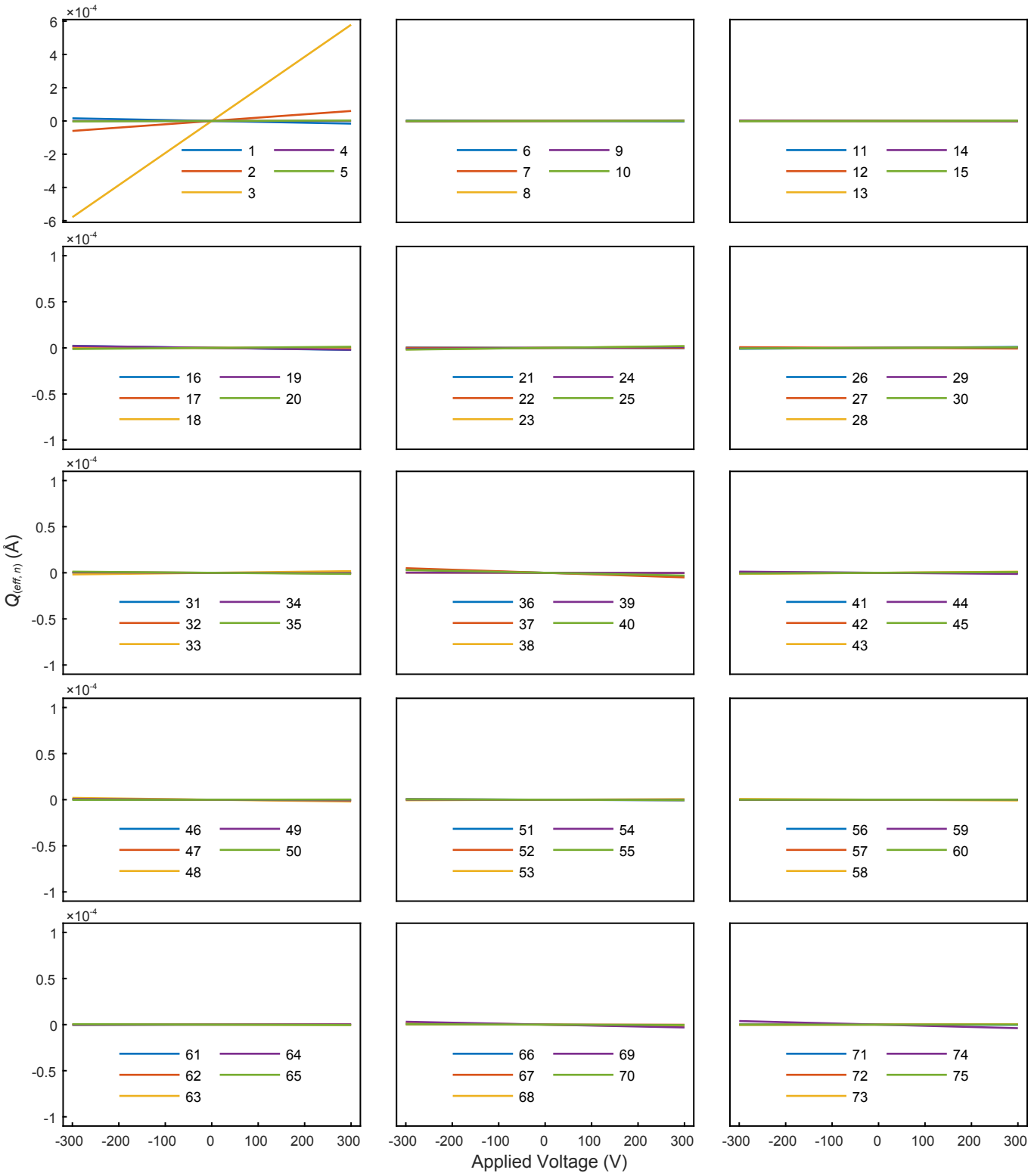

FIG. S17. Effective distortion attained by normal modes 1-75 of the crystal structure at applied voltages.

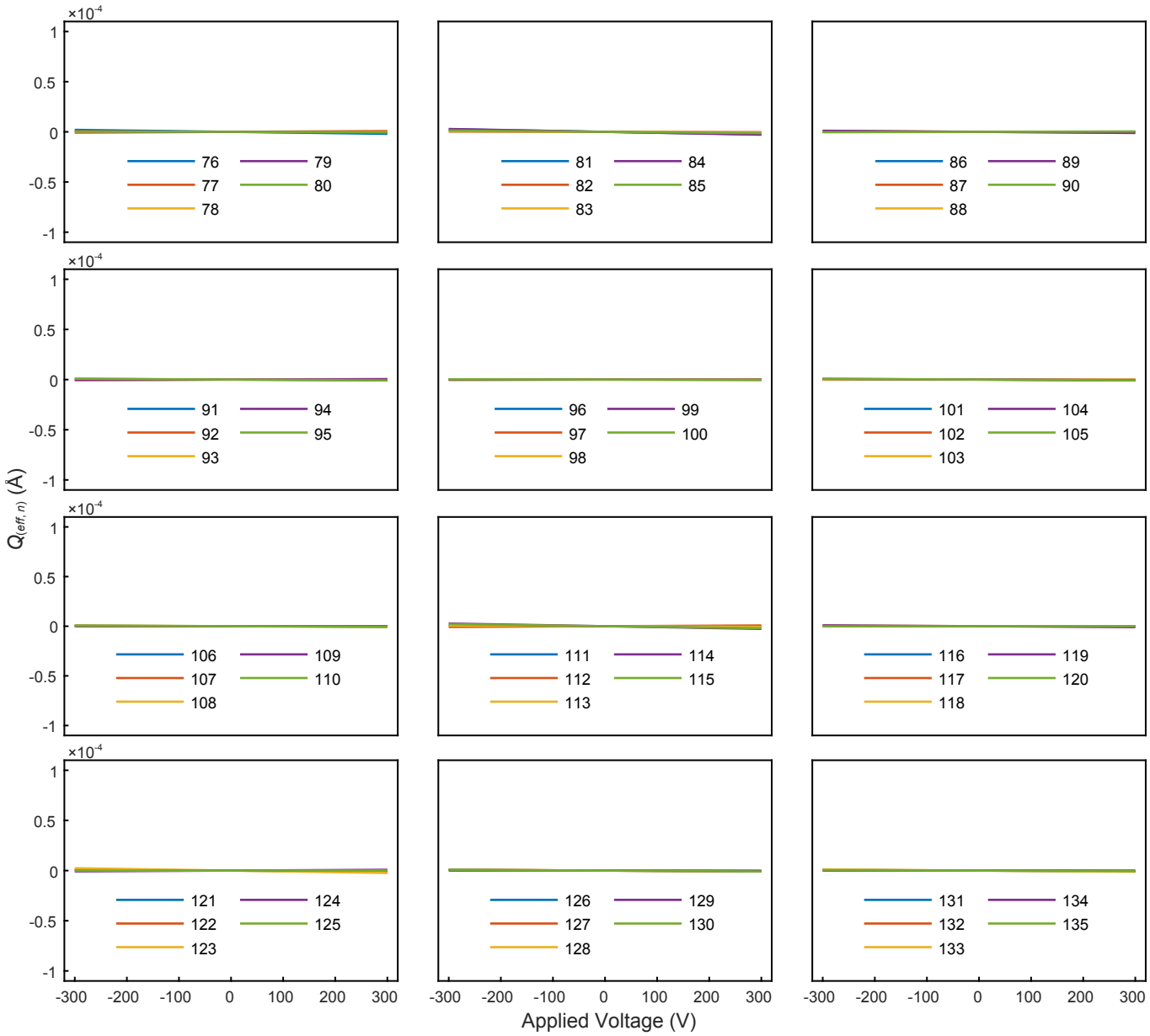

FIG. S18. Effective distortion attained by normal modes 76-135 of the crystal structure at applied voltages.

F. Step 3: Determination of Spin energy Spectrum

Ab-initio calculations were performed to determine the spin energy level scheme, both in terms of the energies and in the composition of the ground state wave function in terms of M_J. Obtained results are provided in Table S5, both at crystallographic geometry and at the relaxed geometry.

TABLE S5. Energy level scheme (in cm^{-1}) and predominant M_J microstate of the ground multiplet of the HoW_{10} complex calculated (CASSCF) on the crystalline coordinates (left) and on the optimized coordinates (right).

$E^{(a)}_{CASSCF}(cm^{-1})$	M_J	$E^{(b)}_{CASSCF}(cm^{-1})$	M_J
0.00	$47.5\%\,\|\pm4\rangle$	0.000	$11.2\%\,\|\pm5\rangle + 12.2\%\,\|\pm6\rangle$
0.36	$47.5\%\,\|\pm4\rangle$	0.022	$13\%\,\|\pm5\rangle + 11.6\%\,\|\pm6\rangle$
26.24	$47.2\%\,\|\pm3\rangle$	10.901	$19.2\%\,\|\pm3\rangle$
27.92	$47.2\%\,\|\pm3\rangle$	10.951	$20.7\%\,\|\pm6\rangle + 14.7\%\,\|0\rangle$
50.08	$48.7\%\,\|\pm5\rangle$	17.490	$23.2\%\,\|\pm5\rangle + 10.2\%\,\|\pm1\rangle$
50.31	$48.7\%\,\|\pm5\rangle$	17.512	$24.6\%\,\|\pm4\rangle + 17.3\%\,\|0\rangle$
86.70	$48.2\%\,\|\pm2\rangle$	53.364	$26.5\%\,\|\pm7\rangle + 10.7\%\,\|\pm1\rangle$
96.34	$48.2\%\,\|\pm2\rangle$	53.481	$11.9\%\,\|\pm8\rangle + 10.9\%\,\|6\rangle$
155.59	$48.9\%\,\|\pm1\rangle$	63.700	$25.7\%\,\|\pm3\rangle + 10.2\%\,\|\pm1\rangle$
156.90	$48.9\%\,\|\pm1\rangle$	63.707	$16.4\%\,\|\pm4\rangle + 24.2\%\,\|\pm2\rangle$
178.90	$46.6\%\,\|\pm6\rangle$	85.863	$24.2\%\,\|\pm2\rangle + 33.5\%\,\|0\rangle$
179.05	$46.6\%\,\|\pm6\rangle$	85.867	$12.7\%\,\|\pm3\rangle + 31.8\%\,\|\pm1\rangle$
181.88	$94.3\%\,\|0\rangle$	92.193	$22.9\%\,\|\pm8\rangle + 18.6\%\,\|0\rangle$
279.97	$49.3\%\,\|\pm8\rangle$	93.320	$23.9\%\,\|\pm7\rangle + 16.8\%\,\|\pm5\rangle$
279.97	$49.3\%\,\|\pm8\rangle$	124.856	$11.1\%\,\|\pm3\rangle + 11.5\%\,\|\pm1\rangle$
315.99	$49.1\%\,\|\pm7\rangle$	126.665	$27.4\%\,\|\pm8\rangle$
315.99	$49.1\%\,\|\pm7\rangle$	138.346	$20.3\%\,\|\pm8\rangle + 10.3\%\,\|\pm6\rangle$

G. Step 4: Effects of the E-field on the tunneling splitting

Finally, we were able to determine the change in the clock-transition frequency (δf) by evaluating the evolution of the tunnel splitting at CASSCF level. The calculations were performed for both crystal and optimized structures see Fig. S19. A clear linear evolution of δf is observed for both structures, both compatible with experimental results. For both structures, the strongest SEC is found when the E-field is applied parallel to the molecular electric dipole, as shown in Fig. S19a and b. The DFT calculations show that the molecular electric dipole is tilted 42° and 54° away from the pseudo tetragonal axis for the optimised and crystal structures, respectively.

This difference can be understood by considering the following symmetry considerations. Since a linear effect of the voltage in the tunneling splitting requires a pre-existing inversion symmetry breaking, in an ideal D_{4d} system the effect would be zero in the first order and only present as a second-order contribution. The relaxed geometry is closer to the ideal D_{4d} symmetry compared with the crystal structure (which is influenced by nearby Na^+ counterions and crystallization H_2O molecules) and thus the effect of an external distortion on its tunnel splitting is underestimated.

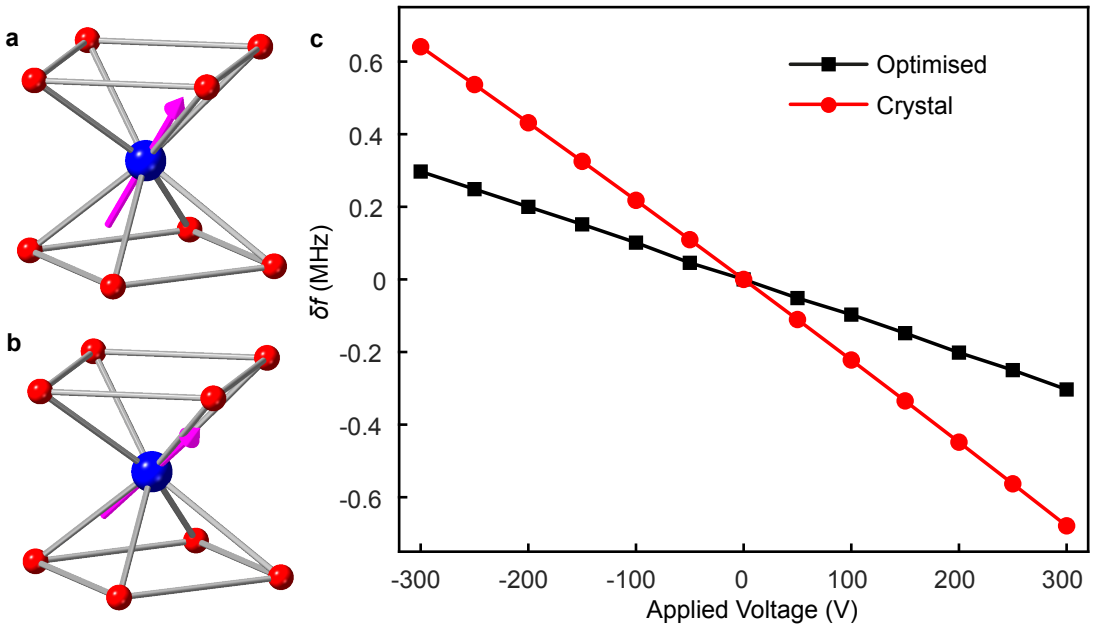

FIG. S19. (a) and (b) The local environment of the Ho, showing the calculated electric dipole direction (magenta arrow) for the optimised and crystal structures, respectively. (c) Change in clock-transition δf as a function of the applied voltage. The black and red symbols correspond to the results calculated using the optimised and crystal structures, respectively.

Additionally we computed the deviation of the easy axis orientation as a function of the applied voltage at CASSCF-SO level (Table S6). At 300 V we obtain deviations of $\delta = 1.27°$ and 0.14° for the optimized and crystallographic structures, respectively. This results in a deviation in the effective field of $\cos(\delta)\cdot B_{\rm CT}$. Since the frequency response is quadratic in the vicinity of the CTs, this translates into changes $k((1-\cos(\delta))\cdot B_{\rm CT})^2$, where $k = 36$ cm^{-1}T^{-2} [S8] and $B_{\rm CT}$ is $B_{\rm min} = 0.0236$, 0.0709, 0.1181 and 0.1654 T. Thus, this effect is in the ranges 1.26×10^{-9} to 6.23×10^{-8} cm^{-1} (optimized) and 2.10×10^{-13} to 1.03×10^{-11} cm^{-1} (crystallographic), i.e. below 0.002 MHz.

TABLE S6. Calculated deviation of the easy axis orientation as a function of the applied voltage.

Voltage (V)	δ_{OPT} (degrees)	δ_{CRYS} (degrees)
-300	-1.276	-0.137
-250	-1.064	-0.115
-200	-0.852	-0.092
-150	-0.639	-0.069
-100	-0.427	-0.046
-50	-0.213	-0.023
0	0.000	0.000
50	0.213	0.023
100	0.426	0.047
150	0.641	0.071
200	0.855	0.096
250	1.070	0.120
300	1.285	0.145

H. Step 5: Calculation of the angular dependency

As a first theoretical estimate of the angular dependence of the transition frequency at the clock transition, we started from Eqn. S15, where ρ is the angle between applied electrical field and the dipole moment.

$$U_n = -\Delta p E \cos\rho \tag{S15}$$

Now, the effective distortion can be obtained by the changing the angle ρ between the applied voltage and the dipole moment.

$$\vec{Q}_{\mathrm{eff}}(V(\rho)) = \sum_n Q_{(\mathrm{eff},n)}(V(\rho)) = Q_{(\mathrm{eff},1)}(V(\rho)) + Q_{(\mathrm{eff},2)}(V(\rho)) + ... + Q_{(\mathrm{eff},3N-6)}(V(\rho)) \tag{S16}$$

We started from the effective distortion obtained at -300V that is $\vec{Q}_{\mathrm{eff}}(-300V(0°))$, and determined further angular dependent distortion at $\vec{Q}_{\mathrm{eff}}(-300V(30°))$, $\vec{Q}_{\mathrm{eff}}(-300V(60°))$, $\vec{Q}_{\mathrm{eff}}(-300V(90°))$, $\vec{Q}_{\mathrm{eff}}(-300V(120°))$, $\vec{Q}_{\mathrm{eff}}(-300V(150°))$ and $\vec{Q}_{\mathrm{eff}}(-300V(180°))$. At each distortion we performed CASSCF-SO calculations to determine the change in clock-transition frequency, obtained results are shown in Fig. S20.

As a proof of concept, if we start from -300V, the obtained electrically induced transition should reach to the value

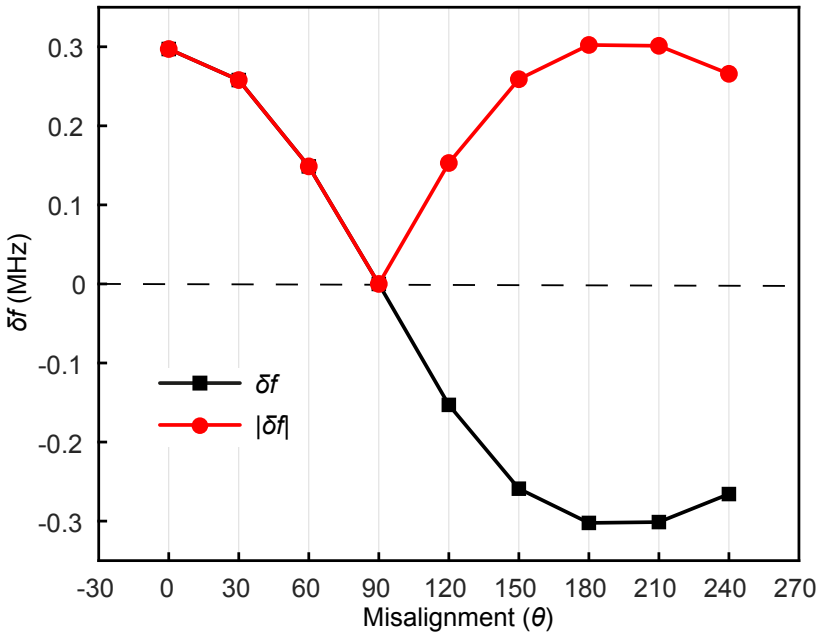

FIG. S20. Change in clock-transition δf (MHz) for angular dependent distortion $\vec{Q}_{\text{eff}}(V(\rho))$ at 300V.

at +300V in linear effect obtained in Fig. S20.

[S1] Casanova, D. *et al.* Minimal distortion pathways in polyhedral rearrangements. *Journal of the American Chemical Society* **126**, 1755–1763 (2004).

[S2] Casanova, D., Llunell, M., Alemany, P. & Alvarez, S. The rich stereochemistry of eight-vertex polyhedra: A continuous shape measures study. *Chemistry – A European Journal* **11**, 1479–1494 (2005).

[S3] Troiani, F. Manipulation of spin cluster qubits by electric field induced modulation of exchange coupling, g-factor, and axial anisotropy. *Physical Review B* **100**, 155424 (2019).

[S4] Forrer, J., García-Rubio, I., Schuhmam, R., Tschaggelar, R. & Harmer, J. Cryogenic Q-band (35GHz) probehead featuring large excitation microwave fields for pulse and continuous wave electron paramagnetic resonance spectroscopy: Performance and applications. *Journal of Magnetic Resonance* **190**, 280–291 (2008).

[S5] Fdez. Galvan, I. *et al.* Openmolcas: From source code to insight. *Journal of chemical theory and computation* **15**, 5925–5964 (2019).

[S6] Ungur, L. & Chibotaru, L. F. Ab initio crystal field for lanthanides. *Chemistry–A European Journal* **23**, 3708–3718 (2017).

[S7] Frisch, M. J. *et al.* Gaussian 16 Revision A.03 (2016).

[S8] Giménez-Santamarina, S., Cardona-Serra, S., Clemente-Juan, J. M., Gaita-Ariño, A. & Coronado, E. Exploiting clock transitions for the chemical design of resilient molecular spin qubits. *Chemical Science* **11**, 10718–10728 (2020).